

Corresponding author: tmyer@crm.cat

## Development and experimental validation of a mathematical model for fluoride-removal filters comprising chemically treated mineral rich carbon

Lucy C. Auton,<sup>1</sup> Shanmuk S. Ravuru,<sup>2</sup> Sirshendu De,<sup>3</sup> Tim Myers,<sup>1</sup> and Abel Valverde<sup>4</sup>

<sup>1</sup>*Centre de Recerca Matemàtica, Campus de Bellaterra, Barcelona, Spain*

<sup>2</sup>*Dept. Chem. & Mat. Eng., University of Alberta, Canada*

<sup>3</sup>*Dept. Chem. Eng., Indian Institute of Technology Kharagpur, India*

<sup>4</sup>*Dept. Chem. Eng, Universitat Politècnica de Catalunya, Escola Superior d'Enginyeries Industrial, Aeroespacial i Audiovisual de Terrassa, Spain*

### Abstract

Excessive fluoride intake can lead to dental and skeletal fluorosis, among other health issues. Naturally occurring fluoride and industrial runoff can result in concentrations far exceeding the World Health Organization's recommended limits in water supplies. In this study, we derive a model incorporating the dominant mechanisms governing fluoride removal from drinking water using the two adsorbents mineral-rich carbon (MRC) and chemically treated mineral-rich carbon (TMRC). Using both new and previously published experimental data, we validate the model for MRC, TMRC, and their mixture, using both batch and column data. Despite the filters containing approximately 40:1 MRC:TMRC ratio by mass, we find that TMRC dominates fluoride removal, while MRC contributes at early and late times. The full column model, which uses parameters from isotherm batch studies, achieves excellent agreement with experimental breakthrough data across varying inlet concentrations and flow rates ( $R^2 > 0.991$ ,  $SSE < 0.0632$ ). Motivated by this, we propose a reduced model based solely on TMRC adsorption, with a single fitting parameter, which still performs well across all breakthrough curves ( $R^2 > 0.983$ ,  $SSE < 0.117$ ). The simplicity of this model means that it is straightforward and inexpensive to work with numerically. In both models, batch and column behaviours are reconciled and, for the case of breakthrough curves with varying inlet concentrations, a set of globally optimised parameters is found. The strong agreement with experimental data supports the model's robustness and reinforces the physical interpretability of its parameters. These models for MRC and TMRC provide a foundation for filter optimisation and future efforts aimed at improving fluoride removal in resource-limited settings.

## I. INTRODUCTION

Fluoridation of drinking water is commonplace with an estimated 5.7% of the global population consuming water with added fluoride [16]. Countries including the United States, Canada, Ireland, Chile and Australia fluoridate over 50% of their water; for example in the United States nearly 60% of the population receiving fluoridated water [16]. The primary motivation for water fluoridation is the prevention of dental caries, as small amounts of fluoride ( $F^-$ ) are essential for healthy teeth and bone development. For this reason, many toothpastes also contain fluoride [30]. However, excessive fluoride intake can lead to adverse health effects, including dental and skeletal fluorosis, and has been linked to other conditions such as cancer, gastrointestinal distress, and neurological damage [7, 30]. Fluoride is naturally present in certain rocks and soils and can leach into groundwater; it can also enter the environment through industrial runoff and atmospheric aerosols, impacting ecosystems [43]. In India, approximately 62 million people are estimated to consume water containing more than the World Health Organization’s (WHO) recommended maximum concentration of 1.5 mg/l ( $\sim 7.89 \times 10^{-5}$  mol/l) of  $F^-$  [59]. This has led to both skeletal and dental fluorosis becoming endemic in India in at least 20 states.

In this paper, we investigate fluoride adsorption filters composed of mineral-rich carbon (MRC) and chemically treated mineral-rich carbon (TMRC) which are currently being sold to the Indian government and distributed across West Bengal. Figure 1 shows examples of prototype and commercial filters at both household and community scales. The commercial community scale filter (Figure 1d), is powered by solar panels. The water filters through various columns, including the mixture of MRC and TMRC and a column of activated carbon which is known for its antibacterial properties. Thus, as well as removing fluoride, the filter additionally removes iron and reduces the bacteria present in the water. Fluoride levels in household wells in the region vary widely—even wells located within a few hundred meters of each other can differ drastically.

Our goal is to understand the chemical processes occurring within filters comprising MRC and TMRC and to develop accurate, predictive models that capture the dominant reactions involved in fluoride removal. Such models enable reliable predictions under varying experimental conditions and facilitate practical applications. This predictive power supports optimisation of filter design, extending operational life and improving cost-efficiency—ultimately contributing to improved access to safe drinking water, a critical goal for sustainable development and public health.

Both TMRC and MRC have proven highly effective in removing fluoride from water. Chatter-

jee et al. [14] report that TMRC— referred to therein as chemically treated carbonised bone meal (CTBM)— has an adsorption capacity of 150 mg/g, significantly outperforming other bio-based adsorbents such as aluminium-treated activated bamboo charcoal (21.1 mg/g) [58]. Mineral rich carbon— referred to as carbonised bone meal or CBM in [13]— exhibits an adsorption capacity of 14 mg/g. Among 102 adsorbents reviewed by Bhatnagar et al. [8], only four outperform TMRC: nanomagnesia, CaO nanoparticles, calcined Mg-Al-CO<sub>3</sub>, and Fe-Al-Ce trimetal oxide.

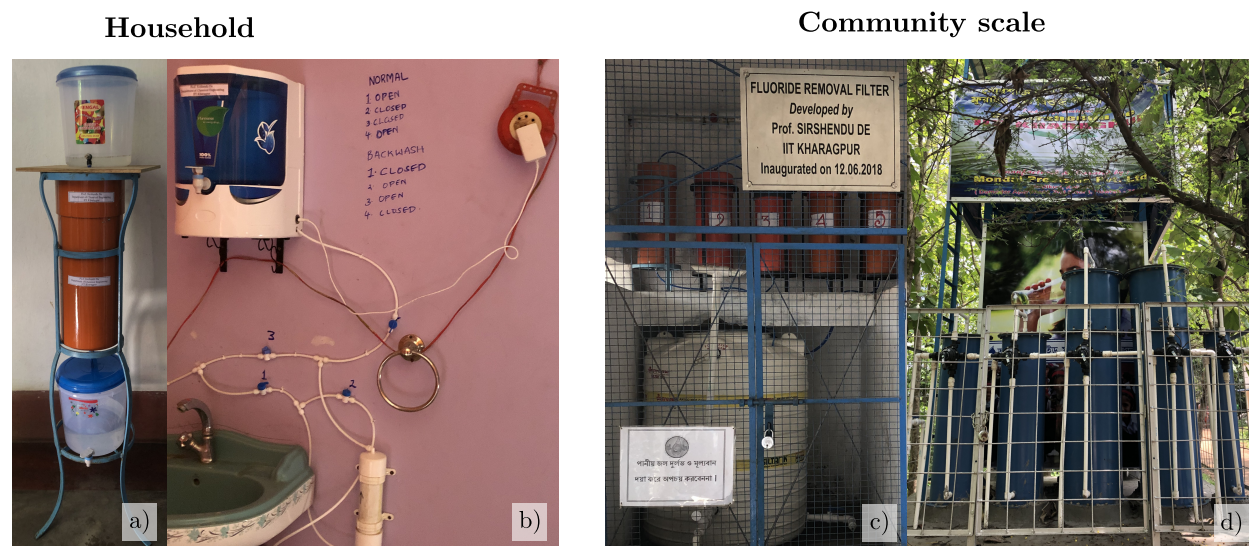


Figure 1: Photos of four different fluoride-removal filters in situ in West Bengal: a) A prototype for a household filter. b) A commercialised version of the household filter c) A prototype for a community-scale filter, situated in a school d) A solar powered, community-scale, commercial filter in a rural village.

Chatterjee et al. [14] modelled TMRC adsorption using Langmuir, Freundlich, and Dubinin–Radushkevich isotherms combined with a dual-porosity kinetic model for column data, though they failed to achieve a good fit. Similarly, for MRC, they applied the same isotherms but employed the Yoon–Nelson model for column studies [13]. Mathematically the isotherm derives from the steady-state of the kinetic model, hence the use of dual-porosity or Yoon–Nelson with unrelated isotherms is inconsistent and this has been shown to result in a poor fit to experimental data or alternatively force system constants to vary with operating parameters, see [38, 40].

Mineral rich carbon, is also known as carbonised bone meal or, equivalently, bone char. Alkurdi et al. [2], Huyen et al. [27], Medellin-Castillo et al. [34], find that approximately 70% – 90% of bone char (MRC) comprises hydroxyapatite and they state that it is the hydroxyapatite in the bone char which is predominantly responsible for the uptake of fluoride. Russo et al. [48] present a

model for fluoride adsorption on hydroxyapatite both for batch and column adsorption using the Adsorption Dynamic Intraparticle Model (ADIM), derived in Russo et al. [47] and based on Do [19]. This model incorporates mass conservation in bulk flow and intra-particle diffusion through both liquid in the ‘pores’ and the ‘solid’ phase, assuming local equilibrium represented by a Freundlich isotherm. However, several inconsistencies arise raising doubt as to whether the mechanics of the system can be effectively predicted using their model.

The present work stems from the preliminary study described in the conference paper of Auton et al. [3]. In this previous work we presented, but did not derive, batch models for fluoride removal by MRC and TMRC and column sorption models for their mixture and showed that they matched experimental data far better than Langmuir’s model, particularly under physically realistic conditions - the focus was on the comparison with Langmuir’s model, with minimal context given, limited analysis and results which address only this comparison. Here, we give the complete story; in addition to providing significantly more background information and context than is contained within [3], we present a careful derivation of the models for MRC and TMRC based on their distinct chemical structures, presenting chemical reactions involved in the removal process and justifying our choice of dominant reactions (MRC: §II B 1, TMRC: §II B 3).

The individual adsorbents are first characterised through batch isotherm and kinetic experiments (MRC: §II B 2, TMRC: §II B 4), and the resulting models are then combined into a model for column filters comprising a mixture of MRC and TMRC (§III). We have also reduced the number of batch isotherm fitting parameters by two, resulting in four intrinsic parameters — as opposed to the six employed in [3]— to be fixed by batch isotherm data. We now do not fit any quantities that are directly measurable and the model is consistent with all modelling assumptions. Further, the present work includes previously unpublished experimental data which investigates the effect of varying flow rate in a column filter; we investigate the adsorption behaviour within the filter and consider all quantities at the filter outlet, not just the concentration of fluoride as was the only outlet quantity discussed in [3].

The following model shows strong agreement with breakthrough curves from column experiments, accurately capturing system behaviour across a range of inlet concentrations and flow rates ( $R^2 > 0.991$ ,  $SSE < 0.0632$ ). Most notably, it accurately captures changes in breakthrough behaviour as the inlet fluoride concentration is varied, without requiring model refitting. Column study results confirm that TMRC is the dominant adsorbent, allowing for a reduced version of the model with only a single fitting parameter (this was not considered in [3]). Despite its simplicity,



the reduced model — with just one fitting parameter — still closely matches experimental results ( $R^2 > 0.983$ ,  $SSE < 0.117$ ), supporting its use as a computationally inexpensive, efficient and robust predictive tool.

## II. CHEMICAL MODEL DERIVATION AND VALIDATION WITH BATCH EXPERIMENTS

We consider the filtration of water contaminated with the passive solute fluoride, ( $F^-$ ), by the adsorbents MRC [13], and TMRC [14]; MRC is carbonised mammalian or avian bone meal, while TMRC is a derivative of MRC which has been chemically treated to improve its fluoride adsorption capacity. The TMRC is made by grinding down MRC and coating it in Aluminium Hydroxide ( $Al(OH)_3$ ). This treatment process makes TMRC more expensive than MRC, since the cost of aluminium significantly exceeds the cost of bone meal. Further, TMRC has an average grain size of 0.1–0.3 mm which is notably smaller than MRC, which has an average grain size of 0.4–0.6 mm [14]: the smaller the grain size the more prone the filter is to clogging. As a result a filter made of pure TMRC would be undesirable. We consider experimental data from two different types of filter: batch filters, which are predominantly experimental tools (Figure 2, left) and column filters, which is the type of filter used in practice (Figure 2, right).

### A. Materials and methods

Chatterjee et al. [12–14] describe the creation of MRC and TMRC and provide a full analysis of their properties - the experiments presented in the current work follow the methodology of [13, 14]. Two different experimental setups are considered: batch (Figure 2, left) and column (or fixed-bed) adsorption experiments (Figure 2, right). We use the batch experiments to determine the intrinsic properties of the fluid–adsorbate–adsorbent system, while both prototype and commercialised filters are employed as column filters. All experiments are carried out with a fluoride solution in the absence of other competing ions (such as calcium, aluminium, nitrate, sulfate, phosphate or chloride).

In batch experiments a contaminated fluid, with a known concentration of fluoride  $c_F$ , is added to a beaker (Figure 2, left) which contains a fixed dose (g/l) of adsorbent. The dose determines the ratio of adsorbent to fluoride-contaminated water. This forms a closed system so that all changes in  $c_F$  are due to removal by the adsorbent. The beaker is then placed in a shaker which homogenises

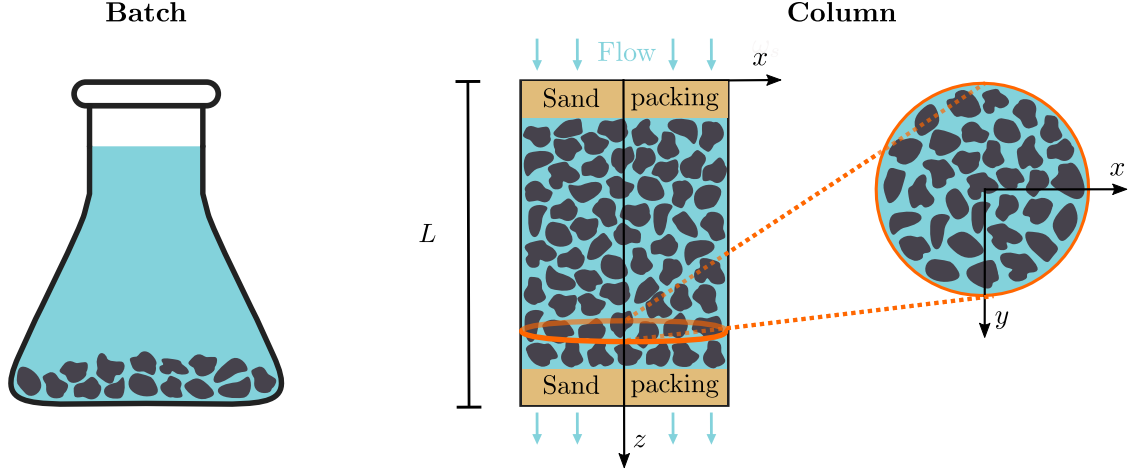


Figure 2: Schematic of batch experiments (left) and column experiments (right). **Left:** A beaker containing a small amount of adsorbent surrounded by contaminated fluid; this forms a closed system with no net flow. **Right:** Contaminated fluid flows through a cylinder evenly packed with an adsorbent. The sand at the inlet and outlet of the filter ensures the water enters the filter uniformly. Note that, the porosity of the packing (and hence fluid fraction) is much lower in column than in batch filters.

the adsorbent-fluid mixture. We use two distinct doses for the batch experiments: for the isotherm experiments 7 g/l of adsorbent is used and only the final equilibrium state is recorded; for the kinetic studies 1 g/l of adsorbent is used and the concentration of fluoride is tracked over time. We use experimental data for both the kinetic and isotherm studies for MRC and TMRC, separately.

For the isotherm study, we record only the final concentration — that is, the beaker remains in the shaker until equilibrium is reached, at which point the adsorbent is filtered from the fluid and the final fluoride concentration is measured yielding a single data point. We repeat this procedure for various initial concentrations, ranging from  $2.5 \times 10^{-4}$  to 0.05 mol/l (4.75 to 950 mg/l). This results in an isotherm curve which relates the equilibrium adsorbed mass of contaminant per unit mass of adsorbent,  $q^e$ , to the corresponding equilibrium fluoride concentration,  $c_F^e$ .

For the kinetic study, the same beaker–shaker setup is used: for MRC  $c_F^i = 5.26 \times 10^{-4}$  mol/l (10 mg/l); for TMRC  $c_F^i = 2.63 \times 10^{-3}$  mol/l (50 mg/l). We measure the fluoride concentration at various times by extracting small fluid samples; each experiment generates a complete kinetic curve.

The column filter consists of a glass cylinder (internal diameter 0.044 m, length 0.25 m) packed with sand at the top and bottom, and, for the column experiments considered in §III, a homogeneous mixture of MRC and TMRC with an approximate mass ratio of 40:1 MRC:TMRC, in be-

tween (Figure 2, right). We allow for small variations in this ratio, with the TMRC fraction taken to lie in the range  $(0.95/41, 1.05/41)$ . The mixture is uniformly packed to a height of  $0.1 \pm 0.005$  m, and fluid flows through the column under gravity at various low flow rates. The inlet pH is fixed at 7, and the ambient temperature is  $300 \pm 3.0$  K. We collect samples at the outlet at regular intervals, measuring the fluoride concentration,  $c_F^{\text{out}}$ , in these sample using an ion-selective electrode.

## B. Batch modelling

In Auton et al. [3], we presented a chemically based model for MRC and TMRC, merely asserting dominant chemical reactions. Here, we carefully derive these models, appealing to the different underlying chemical mechanisms at play and considering the many different chemical reactions that occur during the fluoride sorption process. We then appeal to chemistry to justify the choice of dominant reactions. As in [3], we keep the mechanics of the system simple, instead focusing on the underlying chemistry. We model the filter as a homogeneous porous material with material properties determined via experiments and assume the flow to be unidirectional or ‘plug flow’.

Batch experiments involve a closed system, as such the only change in  $c_F$  is via adsorption on the surface of the adsorbent. Note that in batch experiments the beaker is placed in a shaker which corresponds to a modelling assumption that the system is reaction-limited rather than transport-limited—that is, the only change in concentration is due to the sorption.

### 1. MRC: model derivation (CB-MRC model)

As discussed earlier, Alkurdi et al. [2], Huyen et al. [27], Medellin-Castillo et al. [34], find that approximately 70% – 90% of bone char (MRC) comprises hydroxyapatite and that it is the hydroxyapatite in the bone char which is predominantly responsible for the uptake of fluoride. Hydroxyapatite typically consists of ten calcium ( $\text{Ca}^{2+}$ ) ions, six phosphate ( $\text{PO}_4^{3-}$ ) molecules and two hydroxide ( $\text{OH}^-$ ) molecules (see Figure 3).

To obtain information about hydroxyapatite such as the structure of the lattice, potential substitutions/defects (*e.g.*,  $\text{F}^-$  replacing  $\text{OH}^-$ ), hydrogen bonding, water content, and ion mobility, a solid-state Nuclear Magnetic Resonance (NMR) can be conducted. Mosiman et al. [37] present NMR experiments conducted on hydroxyapatite, which reveal a primary peak attributed to com-

Mineral rich carbon (MRC)



Chemical structure of MRC

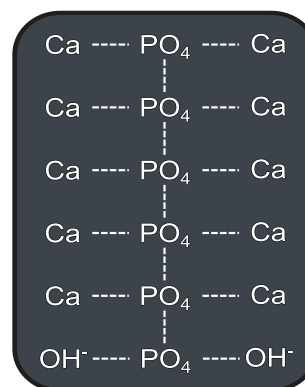


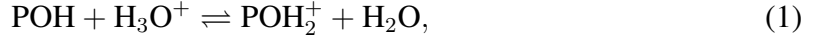
Figure 3: **Left:** photo of MRC before it is sieved to have grain sizes ranging from 0.4–0.6 mm. **Right:** schematic of the chemical structure of MRC.

plexation or ion-exchange and additionally, a second spectral peak consistent with hydrogen bonding. Such experimental evidence contributes to the understanding of how fluoride interacts with hydroxyapatite, supporting various adsorption mechanisms proposed in the literature. The most generally accepted mechanisms are:

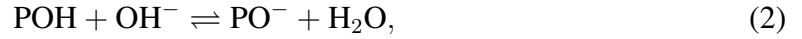
- i. **Complexation<sup>1</sup> and/or ion-exchange with  $\text{OH}^-$  ions (chemisorption):** Mosiman [36], Mosiman et al. [37], and Sternitzke et al. [50] conduct characterization experiments on hydroxyapatite to determine its structure, properties, and composition. These experiments, including the NMR study conducted by Mosiman et al. [37], show that  $\text{OH}^-$  ions in hydroxyapatite can be replaced by  $\text{F}^-$  ions, either through the formation of  $\text{Ca-F}$  complexes in which fluoride is coordinated by multiple  $\text{Ca}^{2+}$  ions, or via a thermodynamically favourable ion-exchange mechanism. Sternitzke et al. [50] report that this replacement primarily occurs at the surface, while Mosiman et al. [37] argue that there is limited support for this in the literature and present evidence that both mechanisms can occur within the hydroxyapatite lattice. The ion-exchange mechanism has also been reported in numerous other works [*e.g.*, 2, 4, 51, 52].
- ii. **Adsorption via intermolecular forces (physisorption):** Huyen et al. [27] and Alkurdi et al. [2] indicate electrostatic attraction between the adsorbent surface and fluoride as one pos-

<sup>1</sup> Complexation is the reversible formation of a coordination complex, which is a chemical compound composed of a central atom or ion—typically a metal—that binds surrounding molecules or ions, called ligands (or complexing agents), such as fluoride, via coordinate covalent bonds.

sible adsorption mechanism. This mechanism can be observed under acidic conditions; the adsorbent surface becomes positively charged via the reaction



where POH represents a surface hydroxyl group on the hydroxyapatite lattice [34]. However, under alkaline conditions, the surface becomes negatively charged according to the reaction



in which case, Medellin-Castillo et al. [34] and Huyen et al. [27] report that electrostatic interaction with fluoride is unlikely.

The NMR experiment conducted by Mosiman et al. [37] supports the works by Sundaram et al. [51] and Balasooriya et al. [4] which indicate that fluoride can also form hydrogen bonds with surface hydroxyl groups on hydroxyapatite. Further, these NMR experiments also corroborate the formation of water molecules within the hydroxyapatite lattice under alkaline conditions, as described by Equation (2).

- iii. **Dissolution-Precipitation:** Numerous studies report that hydroxyapatite can dissolve, releasing calcium ( $\text{Ca}^{2+}$ ) and phosphate ( $\text{PO}_4^{3-}$ ) ions into the aqueous solution [2, 26, 36, 37, 46, 50, 54]. If the solution becomes saturated with these ions and fluoride ( $\text{F}^-$ ) is present in sufficient concentration, calcium fluoride ( $\text{CaF}_2$ ) can precipitate, resulting in a decrease in  $\text{F}^-$  concentration in the solution. However, this phenomenon has typically only been observed under strongly acidic conditions, and significantly higher fluoride concentrations are required for  $\text{CaF}_2$  precipitation to occur at higher pH levels. For example, Ren et al. [46] and Tung and Skrtic [54] indicate that at pH 4, a minimum fluoride concentration of 0.005 mol/l is necessary for precipitation. Characterization studies by Ren et al. [46] further show that at neutral pH, a fluoride concentration of at least 0.1 mol/l (1900 mg/l) is needed for this precipitation to occur. This increases to 0.5 mol/l (9500 mg/l) at pH 10.

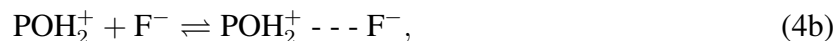
Appealing to the reactions proposed by Alkurdi et al. [2], Balasooriya et al. [4], Sundaram et al. [51], Tomar et al. [52], Tung and Skrtic [54], we conclude that the ion-exchange reactions

occurring within the MRC lattice can be represented as:



where ‘P’ denotes a reactive site in the MRC lattice, typically associated with phosphate groups. As reported by Mosiman et al. [37], both ion-exchange and complexation mechanisms involve substitution of  $\text{OH}^-$  in the lattice and result in chemisorbed fluoride. Hence, Equations (3a) and (3b) can be viewed as global representations of both processes.

According to expressions proposed by Balasooriya et al. [4], Medellin-Castillo et al. [34], Sundaram et al. [51], Tomar et al. [52], physical interactions (physisorption) relevant to MRC include:



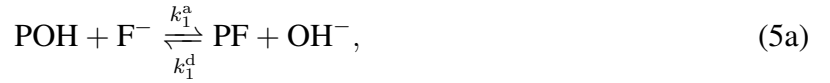
where  $\cdots$  represents hydrogen bonding and  $\text{---}$  represents an electrostatic interaction. Note that these physisorption mechanisms occur at different locations than the chemisorption processes in Equations (3a) and (3b). As reported by Mosiman et al. [37], hydrogen-bonded fluoride may occupy surface or defect sites, while chemisorbed fluoride replaces lattice-bound  $\text{OH}^-$  groups. The electrostatic attraction described in Equation (4b) typically occurs at the positively charged adsorbent surface under acidic conditions [2, 26, 34].

We now turn to the evidence presented in the literature (*cf.* points i, ii, and iii), as well as the operating conditions of the experimental tests conducted in this work (Section II A), to identify the dominant mechanisms governing fluoride removal. All experiments— batch isotherm, batch kinetic, and column— were initiated at pH 7. The point of zero charge ( $\text{pH}_{\text{ZPC}}$ ) for MRC and TMRC are 7.6 and 6.7, respectively [14]. Although the starting pH is slightly below the  $\text{pH}_{\text{ZPC}}$  for MRC, the adsorbent surface can be considered nearly neutral at the outset. However, due to the rapid release of  $\text{OH}^-$  ions, the surface quickly acquires a negative charge via deprotonation (Eq. 2), resulting in an alkaline environment. An immediate consequence of this shift is that the dominant fluoride species in solution remains  $\text{F}^-$  over the entire operational pH range ( $\text{pH} \geq 7$ ) [10]. Further, dissolution–precipitation reactions (point iii) can be excluded as contributing mechanisms, since the maximum fluoride concentration used in this study (0.05 mol/l) remains below the threshold required for such reactions to occur at  $\text{pH} \geq 7$  (0.1 mol/l) [46].



The formation of  $\text{POH}_2^+$  is improbable, as it occurs primarily under acidic conditions [49, 56]. Therefore, we neglect Equations (3b) and (4b), retaining only Equations (3a) and (4a). This simplification is supported by Figure 10, which shows an initial spike in  $\text{OH}^-$  concentration that later subsides, indicating the early onset of deprotonation.

The inhibitory effect of  $\text{OH}^-$  on fluoride adsorption is reflected in the reversible chemisorption reaction (Eq. 3a), where  $\text{OH}^-$  appears on the product side. This reaction is expected to dominate over physisorption under alkaline conditions due to its greater thermodynamic and kinetic favourability. Thus, we take the following two reactions as the dominate reactions during the adsorption process:



where,  $k_1^a$  and  $k_1^d$  are the forward and reverse rate constants for the chemisorption reaction (Eq. 5a), while  $k_2^a$  and  $\kappa_2^d$  correspond to the forward and reverse rate constants for the physisorption process (Eq. 5b). Note that  $\kappa$  and  $k$  are used to distinguish between rate constants with different units.

Finally, the release of  $\text{OH}^-$  exclusively from the chemisorption pathway aligns with observations reported by Mosiman et al. [37], who found that only about half of the  $\text{F}^-$  uptake resulted in a net  $\text{OH}^-$  loss. This is indicative of the coexistence of both chemisorption and physisorption mechanisms.

Note that, we have neglected the explicit competitive effects between  $\text{OH}^-$  and  $\text{F}^-$  for adsorption sites, particularly those described by Equation (3b). This assumption results from the observation that the formation of negatively charged surface species (*e.g.*,  $\text{PO}^-$ ) introduces electrostatic repulsion that reduces fluoride adsorption. Rather than modelling this repulsive interaction directly, we consolidate its effects into the overall desorption term associated with the chemisorption reaction (Eq. 3a), specifically through the rate constant  $k_{d1}$ . The term  $-k_{d1}q_1c_{\text{OH}}$  effectively captures the reduced fluoride adsorption capacity resulting from  $\text{OH}^-$  competition and surface charge effects. By doing so, we eliminate the need to explicitly track the competitive pathway (Eq. 3b), which is less favourable under alkaline conditions, while still preserving the net effect on fluoride removal kinetics.

Equation (5a) represents a chemical reaction involving complexation/ion-exchange between  $\text{F}^-$  and  $\text{OH}^-$ , while Equation (5b) describes a physisorption process. It is important to note that

although the  $\text{OH}^-$  ions interacting with  $\text{F}^-$  appear identical in both reactions (*i.e.*, POH is used to denote both), the adsorption mechanisms involve distinct types of sites. In Equation (5a),  $\text{F}^-$  replaces  $\text{OH}^-$  through ion-exchange at specific chemical sites. In contrast, in Equation (5b),  $\text{F}^-$  physically adsorbs onto  $\text{OH}^-$  groups by occupying vacant or defect sites in the lattice.

## 2. MRC: comparison with batch experiments (CB-MRC model)

We invoke the law of mass-action to express the reactions (Eqs. 5) as a system of differential equations

$$\frac{\partial c_{\text{F}}}{\partial t} = -\frac{\rho^{\text{B}}}{\phi} \left( \frac{\partial q_1}{\partial t} + \frac{\partial q_2}{\partial t} \right) \equiv -\frac{\rho^{\text{B}}}{\phi} \frac{\partial q_{\text{M}}}{\partial t}, \quad (6a)$$

$$\frac{\partial c_{\text{OH}}}{\partial t} = \frac{\rho^{\text{B}}}{\phi} \frac{\partial q_1}{\partial t}, \quad (6b)$$

$$\frac{\partial q_1}{\partial t} = k_1^{\text{a}} c_{\text{F}} (q_1^{\text{m}} - q_1) - k_1^{\text{d}} c_{\text{OH}} q_1, \quad (6c)$$

$$\frac{\partial q_2}{\partial t} = k_2^{\text{a}} c_{\text{F}} (q_2^{\text{m}} - q_2) - \kappa_2^{\text{d}} q_2, \quad (6d)$$

where  $t$  is time,  $\rho^{\text{B}}$  is the bulk density,  $\phi$  is porosity,  $c_{\text{OH}}$  is the concentration of hydroxide (mol/l),  $q_1$  is the moles of the adsorbate PF formed per mass of MRC (mol/g),  $q_2$  is the moles of the adsorbate  $\text{POH} \cdots \text{F}$  formed per mass of MRC (mol/g),  $q_i^{\text{m}}$  is the maximum attainable value of  $q_i$ , for  $i = 1, 2$  with  $q_{\text{M}} := q_1 + q_2$ . The bulk density of an adsorbent  $\rho^{\text{B}}$  is defined to be the total initial mass of the adsorbent, divided by the total volume of the filter, and the porosity  $\phi$  is defined to be the fluid fraction of the batch filter. Thus, for batch filters the quantity  $\gamma := \rho^{\text{B}}/\phi$  is equivalent to the dose. As such, for the isotherm experiments  $\gamma := \gamma_{\text{iso}} \equiv 7$  and for the kinetic experiments  $\gamma := \gamma_{\text{kin}} \equiv 1$ . Note that the same doses are used regardless of adsorbent and thus, for batch experiments, the value of  $\gamma$  depends only on isotherm vs kinetic and not the particular adsorbent used.

Initially, the MRC is contaminant free; we add a solution to the beaker which contains a known, initial, concentration of  $\text{F}^-$  ( $c_{\text{F}}^{\text{i}}$ ) and an initial concentration of  $\text{OH}^-$  ( $c_{\text{OH}}^{\text{i}}$ ) which is calculated from the pH of the system. Thus, at  $t = 0$ :

$$q_1 = q_2 = 0 \quad (6e)$$

$$c_{\text{F}} = c_{\text{F}}^{\text{i}} \quad (6f)$$

$$c_{\text{OH}} = c_{\text{OH}}^{\text{i}} \quad (6g)$$

where  $c_\star^i$  is the inlet concentration of contaminant where  $\star$  denotes either F or OH. We refer to the chemically based model for MRC as defined in Equations (6) as the CB-MRC model.

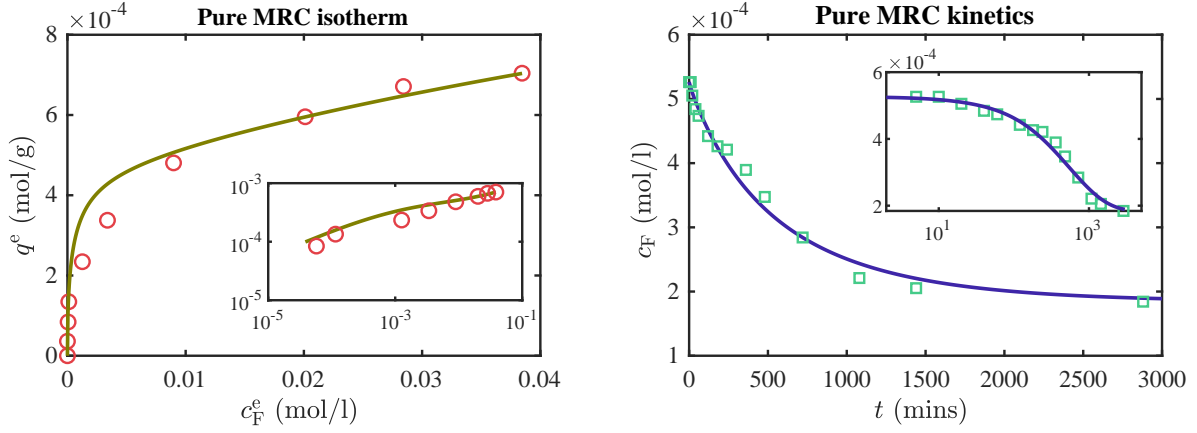


Figure 4: Isotherm (left) and kinetic study (right) for MRC fitted with the CB-MRC model (Eqs. 6) **Left:** All experimental data points (red circles) are the equilibrium values of  $q$  against  $c_F$  for individual experiments, each with a different, known  $c_F^i$ . To examine the fit more closely for small  $c_F^e$ , we also include a log-log plot of  $q^e$  against  $c_F^e$  (inset). **Right:** All experimental data points (green squares) are from the same experiment. To examine the fit more closely at small times, we include a semi-log plot of  $c_F$  against  $t$  (inset).

For the CB-MRC model we solve for the isotherm analytically but the kinetic function numerically in MATLAB<sup>®</sup> using `ode15s`. The isotherm is the equilibrium of the system (Eqs. 6) given by  $q_M = q_M^e \equiv q_1^e + q_2^e$ . At equilibrium Equations (6) reduce to

$$k_1^a(c_F^i - \gamma_{\text{iso}}q_M^e)(q_1^m - q_1) = k_1^d(c_{\text{OH}}^i + \gamma_{\text{iso}}q_1^e)q_1 \quad (7a)$$

$$k_2^a(c_F^i - \gamma_{\text{iso}}q_M^e)(q_2^m - q_2) = \kappa_2^d q_2 \quad (7b)$$

with solution

$$q_1^e := \frac{-(c_{\text{OH}}^i + K_1 c_F^e) + \sqrt{(c_{\text{OH}}^i + K_1 c_F^e)^2 + 4\gamma_{\text{iso}}K_1 c_F^e q_1^m}}{2\gamma_{\text{iso}}} \quad (8a)$$

$$q_2^e := \frac{\mathcal{K}_2 c_F^e q_2^M}{1 + \mathcal{K}_2 c_F^e} \quad (8b)$$

where

$$K_1 := \frac{k_1^a}{k_1^d} \quad \text{and} \quad \mathcal{K}_2 := \frac{k_2^a}{\kappa_2^d} \quad (8c)$$

Further, we use the constraint,

$$q_M^e = \frac{c_F^i - c_F^e}{\gamma_{\text{kin}}}, \quad (9)$$

obtained via integrating Equation (6a), to find  $\mathcal{K}_2$  using the kinetic data:

$$\mathcal{K}_2 \equiv \frac{c_F^i - c_F^e - \gamma_{\text{kin}} q_1^e}{c_F^e [\gamma_{\text{kin}} (q_2^m + q_1^e) + c_F^e - c_F^i]}. \quad (10)$$

Figure 4 presents the experimental data alongside the best fit as obtained from the model defined by Equations (6). The left panel of Figure 4 corresponds to the MRC isotherm, while the right panel shows the results of the MRC kinetic study.

The MRC isotherm requires three fitting parameters:  $K_1$ ,  $q_M^m$  and  $q_2^m/q_M^m$ . These three parameters are fitted for first using just the isotherm. The kinetic curve then requires two further fitting parameter:  $k_1^a$  and  $k_2^a$ . Note that, the three parameters which can be determined using only the isotherm are intrinsic constants of the system and are subsequently used in the column experiments reducing the required number of fitting parameters for the column filter. The remaining two MRC parameters,  $k_1^a$  and  $k_2^a$ , are only used for the kinetic curves. These two parameters must be re-fit for in the column experiments as they are specific to the experimental setup. Our fitting is conducted in MATLAB<sup>®</sup> using the `GlobalSearch` function to minimise the objective function which is the absolute difference between the model predictions and data points, for the isotherm and then subsequently the kinetic curve. Note that MATLAB<sup>®</sup>'s `GlobalSearch` algorithm, which is based on Ugray et al. [55], utilises a stratified-sampling procedure to randomly generate trial points [33]. As a result, each time the same code is run, slightly different optima are produced. To produce the values in Tables I and II we have run the optimisation algorithm multiple times ( $\mathcal{O}(10)$ ) and selected the parameter values which yield the lowest SSE and highest  $R^2$ .

Table I presents the parameter values extracted from the kinetic study (top left) and those calculated from the fitting parameters (bottom left), alongside the five optimized batch parameters (center) and the goodness-of-fit metrics (right). Notably, the initial hydroxide ion concentration,  $c_{\text{OH}}^i$ , is fixed at  $10^{-7}$  mol/l, reflecting the system's pH of 7. The pH is defined chemically as  $\text{pH} = -\log[\text{H}_3\text{O}^+]$ . The hydroxide ion concentration is related to the pOH by  $c_{\text{OH}} = 10^{-\text{pOH}}$ , where  $\text{pOH} = -\log[\text{OH}^-]$ .

The relationship between pH and pOH derives from the self-ionization of water,



MRC isotherm and kinetic parameters								
Extracted (kinetic)			Optimised parameters			Goodness of fit		
Param.	Value	Units	Param.	Value	Units	Param.	Iso./Kin.	Value
$c_F^i$	$5.26 \times 10^{-4}$ (10)	mol/l (mg/l)	$K_1$	4.74	–	SSE	Isotherm	0.0514
$c_{OH}^i$	$1 \times 10^{-7}$ (0.0017)	mol/l (mg/l)	$q_M^m$	0.00174	mol/g	$R^2$	Isotherm	0.961
$c_F^e$	$1.84 \times 10^{-4}$ (3.5)	mol/l (mg/l)	$q_2^m/q_M^m$	0.729	–	SSE	Kinetic	0.0105
Calculated			$k_1^a$	2.78	l/(mol·s)	$R^2$	Kinetic	0.986
$\mathcal{K}_2$	6.00	l/mol	$k_2^a$	0.389	l/(mol·s)			

Table I: Parameters for the chemically based MRC model (CB-MRC, Eqs. 6), where  $q_M^m := q_1^m + q_2^m$ .

**Left (top):** parameter values extracted from the kinetic experiment;  $c_{OH}^i$  is calculated based on the pH of the system which is held at 7. The concentrations are shown in mol/l and in brackets the equivalent in mg/l. **Left (bottom):** the value of  $\mathcal{K}_2$  calculated using the optimised parameters and Equation (10).

**Centre:** Parameters optimised using both the isotherm and kinetic experiments. **Right:** the sum of squares error (SSE) and the coefficient of determination ( $R^2$ ). The  $R^2$  is nondimensional by construction. For the kinetic study we nondimensionalised the SSE with  $c_F^i$ , while for the isotherm, we nondimensionalised the SSE with the largest experimentally determined value of  $q^e$ . Note that to convert  $c_F$  from mol/l to mg/l we must multiply by 19000, while to convert  $c_{OH}$  we must multiply by 17000.

which at room temperature ( $\sim 25^\circ\text{C}$ ) satisfies the approximate relation

$$\text{pH} + \text{pOH} \approx 14. \quad (12)$$

As the initial pH is recorded as 7, it follows that  $\text{pOH} = 7$ , and thus the hydroxide ion concentration is  $c_{OH}^i = 10^{-7}$  mol/l [11].

The equilibrium constant  $K_1$  is order 1, neither particularly high nor low; being nondimensional, this clearly suggests a reversible reaction. In contrast,  $\mathcal{K}_2$  is dimensional, which complicates its direct interpretation. However, given that  $\mathcal{K}_2$  scales with  $1/c_F^e$  and that  $c_F^e$  is very low, one would expect  $\mathcal{K}_2$  to be quite large. The fact that it is instead of order 10 suggests that  $q_2^e$  is also small. This observation is consistent with the presence of a negatively charged surface under alkaline conditions, which tends to hinder physisorption due to its relatively weak interaction forces [26, 34]. Further, the ratio  $q_2^m/q_M^m = 0.637$  indicates a slightly greater number of vacant sites in the hydroxyapatite lattice available for fluoride physisorption compared to hydroxide ions

available for ion-exchange. This ratio being close to one half aligns with the findings of Mosiman et al. [37], who reported that the net loss of  $\text{OH}^-$  is approximately half of the  $\text{F}^-$  uptake. This would imply that physisorption accounts for roughly half of the maximum fluoride removal capacity, with ion-exchange accounting for the remainder.

Regarding model fitting, the coefficient of determination  $R^2$  is, by definition, nondimensional for both the isotherm and kinetic curves. The sum of squared errors (SSE), however, carries units of  $\text{mol}^2/\text{g}^2$  for the isotherm and  $\text{mol}^2/\text{l}^2$  for the kinetic study. To facilitate comparison, the SSE was nondimensionalized: for the kinetic model, this was achieved using the initial concentration  $c_{\text{F}}^{\text{i}}$ , and for the isotherm, using the largest data point in the dataset. These adjustments allow for a meaningful assessment of model performance. The combination of an  $R^2$  value close to 1 and relatively low nondimensional SSE indicates a good fit overall as we have here. However, despite the strong values for SSE and  $R^2$ , in the isotherm some deviation is observed around  $c_{\text{F}}^{\text{e}} \approx 0.005$ , where the curvature of the model slightly diverges from the experimental data (see Figure 4). We hypothesise that this discrepancy may stem from the accumulation of small, systematic errors—for example those related to dosage precision and experimental uncertainties in measurement and mixing. These seemingly minor inaccuracies, when summed, can lead to noticeable deviations in model performance at specific concentration ranges. Further investigation into error propagation and sensitivity analysis could help quantify the extent to which these small errors influence model accuracy.

### 3. TMRC: model derivation (IE-TMRC model)

Chemically-treated mineral rich carbon (TMRC) is made by grinding down MRC and coating it in aluminium hydroxide ( $\text{Al}(\text{OH})_3$ ). This significantly aids in the adsorption of fluoride; the adsorption capacity of TMRC is approximately ten times greater than that of MRC [14]. Thus, we neglect any reaction that occurs in TMRC and does not involve aluminium, including the contribution of the hydroxyapatite core.

The aluminium hydroxide coating layer consists of a crystalline structure that can form coordination complexes with water molecules [18, 25, 32, 42]. The primary chemical and physical mechanisms affecting fluoride adsorption onto the  $\text{Al}(\text{OH})_3$  surface are largely analogous to those proposed for hydroxyapatite. These mechanisms include:

- i. **Complexation and/or ion-exchange with  $\text{OH}^-$  (chemisorption):** Several studies have



### Production of chemically treated MRC (TMRC)



### Chemical structure of TMRC

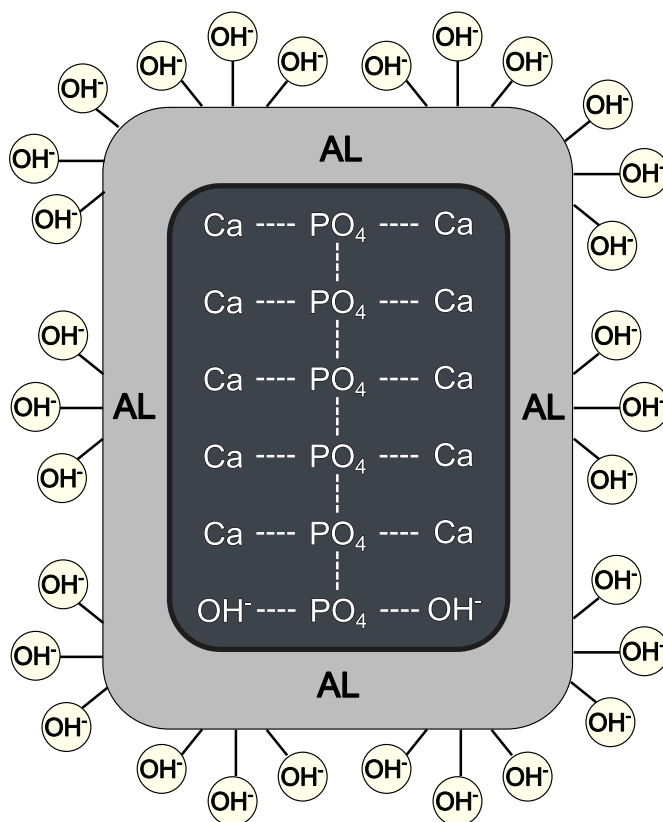


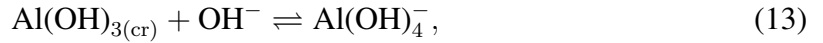
Figure 5: Left: photo showing the prototype procedure for making TMRC from MRC. Right: schematic of the chemical structure of TMRC; showing how the fluoride and hydroxide molecules interact with the TMRC.

reported that fluoride interacts with aluminium hydroxide-based adsorbents, including activated alumina [18, 24, 32] and various aluminium hydroxide polymorphs [23, 42], primarily through surface complexation. This process can alter the local crystalline structure. However, Gong et al. [23] and Ghorai et al. [21] observed that this mechanism predominately occurs at low pH. Under alkaline conditions, fluoride adsorption occurs mainly via ion-exchange between  $F^-$  and surface  $OH^-$  groups, a process that typically preserves the structural integrity of the coating. This ion-exchange mechanism has also been described by [22, 29]. When the  $OH^-$  groups involved are part of a pre-existing surface complex, as is the case here, this is sometimes referred to as ‘ligand exchange’ [5, 15, 20, 53].

- ii. **Adsorption via intermolecular forces (physisorption):** Similar to the mechanism described for MRC, the surface of the TMRC can undergo protonation in acidic media and

deprotonation in alkaline conditions, via analogous reactions to those involving POH but instead involving Al–OH (see reactions (Eq. 1) and (Eq. 2)). Under acidic conditions, electrostatic attraction may facilitate fluoride physisorption. However, under alkaline conditions, such interactions are significantly weakened due to surface deprotonation and electrostatic repulsion [9, 15, 18, 21, 22, 32, 42]. Additionally, hydrogen bonding between fluoride and surface hydroxyl groups has been proposed as a contributing physisorption mechanism [32, 42].

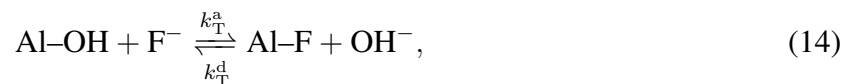
- iii. **Dissolution–precipitation:** It is widely accepted that aluminium-fluoride complexes (*e.g.*,  $\text{AlF}_\alpha^{3-\alpha}$ ) are more soluble under acidic conditions, with minimal dissolution occurring near neutral pH [15, 18, 23, 32, 42]. However, studies using activated alumina [17, 32] and various aluminium hydroxide phases [6, 60] have reported increasing dissolution of fluorohydroxoaluminate species (*e.g.*,  $\text{AlF}_\alpha(\text{OH})_\beta^{3-\alpha-\beta}$ ) with increasing pH. Among these,  $\text{Al}(\text{OH})_4^-$  is often the dominant species. This process is described by the equilibrium reaction:



where  $\text{Al}(\text{OH})_{3(\text{cr})}$  represents the crystalline solid phase of the coating, while  $\text{OH}^-$  and  $\text{Al}(\text{OH})_4^-$  are aqueous species in the surrounding fluid. This dissolution equilibrium is influenced by the competition between  $\text{OH}^-$  and  $\text{F}^-$  ions for surface adsorption sites [15], and may account for the elevated aluminium concentrations observed in the column effluents, as reported by Chatterjee et al. [14].

Analogous to the model development for MRC, we exclude all reactions associated with a positively charged surface. This is justified by the initial pH of 7 and  $\text{pH}_{\text{ZPC}} = 6.7$  for TMRC [14], which suggests that the adsorbent surface becomes negatively charged under operating conditions. Further, the anticipated release of  $\text{OH}^-$  ions is expected to rapidly drive the system into a strongly alkaline environment. For this reason, we assume that the predominant fluoride species in solution remains as  $\text{F}^-$  over the entire operating pH range ( $\text{pH} \geq 7$ ) [10].

In line with assumptions made in deriving MRC model, we assume chemisorption occurs via an ion-exchange or ligand-exchange mechanism between  $\text{OH}^-$  and  $\text{F}^-$  at the aluminium hydroxide surface of the TMRC. Appealing to Chatterjee et al. [14], Gai et al. [20], Ghorai and Pant [21], Tripathy et al. [53], this reaction can be represented as:



where  $k_T^a$  and  $k_T^d$  are the forward and reverse rate constants, respectively. Here, Al–OH represents individual surface bonds between aluminium and hydroxide groups that are displaced by Al–F bonds during fluoride adsorption. Although ion-exchange and ligand-exchange differ mechanistically, both can be described using this global reaction, which defines the chemisorption mechanism outlined in point (i).

Physisorption via hydrogen bonding (point ii) was considered in the MRC model, based on the assumption that the hydroxyapatite lattice contains vacancies and defects capable of hosting  $F^-$  through hydrogen bonding with  $OH^-$  groups [37]. However, TMRC consists of a thin crystalline coating layer, where hydrogen bonding would be limited to surface interactions. Given that electrostatic attraction is already suppressed under alkaline conditions due to surface deprotonation, we assume that surface-level hydrogen bonding is insufficiently strong to contribute meaningfully to fluoride adsorption. As such, physisorption is neglected in the TMRC model.

Finally, for consistency with the MRC model and to simplify the analysis, we neglect competition between  $F^-$  and  $OH^-$  for surface adsorption sites. This implies that dissolution processes occurring at high pH—described in point (iii) and governed by reaction (Eq. 13)—are not included in the model.

#### 4. TMRC: comparison with batch experiments (IE-TMRC model)

We again invoke the law of mass-action to express reaction (Eq. 14) as a system of differential equations [24, 41],

$$\frac{\partial c_F}{\partial t} = -\frac{\rho^B}{\phi} \frac{\partial q_T}{\partial t}, \quad (15a)$$

$$\frac{\partial c_{OH}}{\partial t} = \frac{\rho^B}{\phi} \frac{\partial q_T}{\partial t}, \quad (15b)$$

$$\frac{\partial q_T}{\partial t} = k_T^a c_F (q_T^m - q_T) - k_T^d c_{OH} q_T, \quad (15c)$$

where  $q_T$  is the number of moles of the adsorbate Al–F formed per mass of TMRC (mol/g), and  $q_T^m$  is the maximum attainable value of  $q_T$ . As for MRC  $\gamma := \rho^B/\phi$  with  $\gamma := \gamma_{iso} \equiv 7$  for the

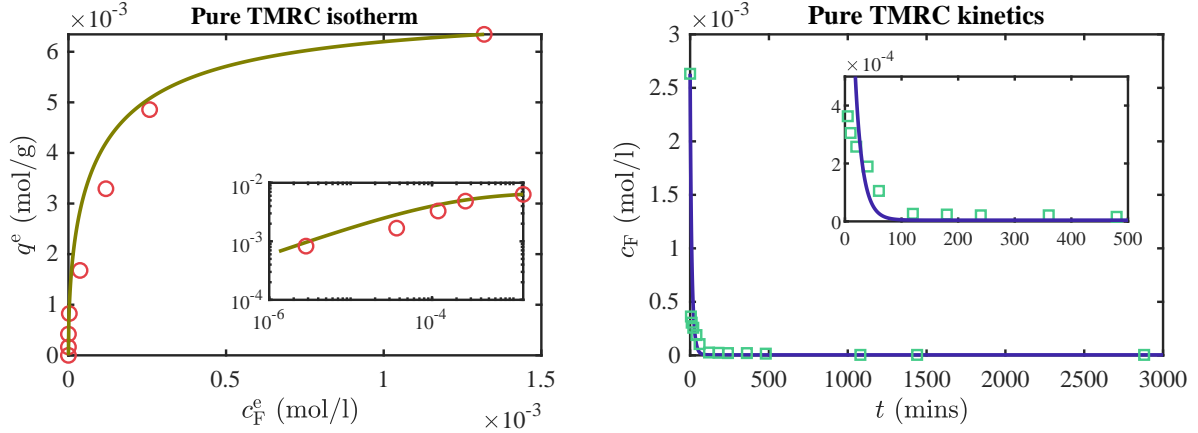


Figure 6: Isotherm (left) and kinetic study (right) for TMRC fitted with both the IE-TMRC model (Eqs. 15). **Left:** To examine the fit more closely for small  $c_F^e$ , we also include a log-log plot of  $q^e$  against  $c_F^e$  (inset). **Right:** To examine the fit more closely at small times, we include a semi-log plot of  $c_F$  against  $t$  (inset).

isotherm experiments and  $\gamma := \gamma_{\text{kin}} \equiv 1$  for the kinetic experiments and, as before, at  $t = 0$ ,

$$q_T = 0, \quad (15d)$$

$$c_F = c_F^i \quad (15e)$$

$$c_{\text{OH}} = c_{\text{OH}}^i. \quad (15f)$$

As in the case of MRC, the inhibitory effect of  $\text{OH}^-$  on fluoride adsorption is inherently accounted for by the presence of  $\text{OH}^-$  on the product side of the reversible chemisorption reaction (Eq. 14). However, for TMRC, it is possible that some of the released hydroxide is not present as free  $\text{OH}^-$  ions, but rather as hydroxyl groups complexed in the form of  $\text{Al}(\text{OH})_4^-$ , as suggested by Equation (13). This interpretation is consistent with the findings reported by Chatterjee et al. [14].

We refer to the ion-exchange model for TMRC as defined in Equations (15) as the IE-TMRC model. For the IE-TMRC model, we solve for both the isotherms and kinetic functions analytically. For the kinetic result we express Equation (15c) as

$$\frac{dq_T}{dt} = A(q_T - R_+)(q_T - R_-) \quad (16a)$$

where

$$A := \gamma_{\text{kin}}(k_T^a - k_T^d) \quad \text{and} \quad R_{\pm} := \frac{B \pm \sqrt{B^2 - 4AD}}{2A} \quad (16b)$$

with

$$B := k_T^a(\gamma_{\text{kin}}q_T^m + c_F^i) + k_T^d c_{\text{OH}}^i \quad \text{and} \quad D := k_T^a c_F^i q_T^m. \quad (16c)$$

Solving Equations (16) yields

$$q_T = \frac{R_- R_+ \{ \exp[-A(R_+ - R_-)t] - 1 \}}{R_- \exp[-A(R_+ - R_-)t] - R_+}, \quad (16d)$$

where  $c_F$  is given by

$$c_F = c_F^i - \gamma_T q_{\text{kin}}. \quad (16e)$$

The isotherm is determined via the equilibrium of Equation (15c), yielding

$$q_T^e = -f_1(c_F^e) + \sqrt{[f_1(c_F^e)]^2 + f_2(c_F^e)} \quad (17a)$$

where

$$f_1(c_F^e) := \frac{c_{\text{OH}}^i + K_T c_F^e}{2\gamma_{\text{iso}}}, \quad f_2(c_F^e) := \frac{q_T^m K_T c_F^e}{\gamma_{\text{iso}}} \quad \text{and} \quad K_T := \frac{k_T^a}{k_T^d} \quad (17b)$$

We use the constraint

$$\gamma_{\text{kin}} q_T^e = c_F^i - c_F^e \quad (18)$$

which results from integrating Equation (15a) to determine  $K_T$  in terms of the other parameter

$$K_T = \frac{(c_F^i - c_F^e)(c_F^i - c_F^e + c_{\text{OH}}^i)}{c_F^e(\gamma_{\text{kin}} q_T^m - c_F^i + c_F^e)}. \quad (19)$$

Figure 6 shows the experimental data and the best fit as predicted by the model defined in Equations (15). The left panel of Figure 6 corresponds to the TMRC isotherm, while the right panel shows the results of the TMRC kinetic study.

TMRC isotherm and kinetic parameters								
Extracted (kinetic)			Optimised parameters			Goodness of fit		
Param.	Value	Units	Param.	Value	Units	Param.	Iso./Kin.	Value
$c_F^i$	$2.63 \times 10^{-3}$ (50.0)	mol/l (mg/l)	$q_T^m$	0.0069	mol/g	SSE	Isotherm	0.0615
$c_{\text{OH}}^i$	$1 \times 10^{-7}$ (0.0017)	mol/l (mg/l)	$k_T^a$	16.5	l/(mol·s)	R <sup>2</sup>	Isotherm	0.938
$c_F^e$	$4.21 \times 10^{-6}$ (0.08)	mol/l (mg/l)	Calculated			SSE	Kinetic	0.283
			$K_T$	384	–	R <sup>2</sup>	Kinetic	0.680

Table II: Parameters of the ion-exchange model for TMRC (IE-TMRC, Eqs. 15). The same groups of parameters are presented as in Table I (*i.e.*, Extracted, Optimised parameters, Calculated and Goodness of fit). Further, the goodness of fit parameters have been nondimensionalised as in Table I

There are two fitting parameters for TMRC:  $q_T^m$  which is fitted from the isotherm, and  $k_T^a$  which is subsequently fitted from the kinetic study. As before, all fittings are via the `GlobalSearch` function in `MATLAB`® such that the objective function is the absolute difference between the model predictions and data points. As for the CB-MRC model,  $q_T^m$  is an intrinsic constant of the system, while  $k_T^a$  must be re-fit for the column experiments as it is specific to the experimental set-up.

Table II presents the parameter values extracted from the kinetic study (left) and those calculated from the fitting parameters (centre, bottom), alongside the two optimized batch parameters (centre, top) and the goodness-of-fit metrics (right).

Given that  $K_T$  is dimensionless and relatively large (order of hundreds), it suggests that the chemisorption reaction undergone by the TMRC is relatively direct, with a stronger forward (adsorption) tendency than reverse (desorption), implying a quasi-irreversible behaviour. This interpretation is consistent with experimental observations indicating that TMRC exhibits a greater affinity for fluoride compared to MRC [14], effectively functioning as a more efficient adsorbent. Further, the maximum adsorption capacity  $q_T^m$  is approximately one order of magnitude greater than  $q_M^m$ , which aligns with the reported finding that TMRC absorbs roughly ten times more than MRC [14].

Figure 6 (left panel) demonstrates a good fit of the equilibrium isotherm to the experimental data, as indicated by a low sum of squared errors (SSE = 0.0615) and a high coefficient of determination ( $R^2 = 0.938$ ). The right panel shows the kinetic profile, which also aligns reasonably well with the observed data. However, the early-time region exhibits a rapid transition, indicating that the majority of fluoride uptake occurs within a short initial period. This sharp adsorption front introduces potential measurement uncertainties, as the rate of fluoride removal may exceed the temporal resolution of the sampling process. We hypothesise that this initial transient is responsible for the comparatively higher SSE (0.283) and the moderate  $R^2$  value (0.68) observed in the kinetic fit. Nevertheless, it is important to note that the parameters obtained from these batch experiments yield a good agreement when applied to the column experiments, supporting the robustness of the model.



### III. COLUMN FILTER

We consider the steady flow of fluid contaminated with  $F^-$  through a column filter, modelled as a homogeneous porous medium. We assume unidirectional (plug) flow, as such the fluid flow moves parallel to the  $z$ -axis (aligned vertically downward) with a constant Darcy velocity  $v$ . The contaminated water enters uniformly at the inlet,  $z = 0$ , and exits at the outlet,  $z = L$ . The inlet concentrations of fluoride and hydroxide ions are controlled, while the outlet fluoride concentration,  $c_F^{\text{out}}$ , is measured as a function of time; the graph of  $c_F^{\text{out}}$  vs  $t$  is known as a breakthrough curve. Note that, in this section we consider concentrations solely in units of mg/l rather than mol/l; the conversion between the units is the same as detailed in Table I.

In column filters, the dominant mechanisms for contaminant transport are advection and hydrodynamic (shear) dispersion. For the MRC–TMRC mixture, we assume fluoride removal occurs via the same chemical reactions as in the batch system, namely those described by Equations (5) and (14) [2, 5, 21, 51, 52]. Accordingly, the sink terms remain identical to those used in the batch model.

Transport of  $F^-$  and  $OH^-$  ions through the filter is modelled by a system of advection–diffusion–reaction equations with removal via both MRC and TMRC components:

$$\frac{\partial c_F}{\partial t} = D_F \frac{\partial^2 c_F}{\partial z^2} - v \frac{\partial c_F}{\partial z} - \left( \frac{\rho_M^B}{\phi_C} \frac{\partial q_1}{\partial t} + \frac{\rho_M^B}{\phi_C} \frac{\partial q_2}{\partial t} + \frac{\rho_T^B}{\phi_C} \frac{\partial q_T}{\partial t} \right), \quad (20a)$$

$$\frac{\partial c_{OH}}{\partial t} = D_{OH} \frac{\partial^2 c_{OH}}{\partial z^2} - v \frac{\partial c_{OH}}{\partial z} + \left( \frac{\rho_M^B}{\phi_C} \frac{\partial q_1}{\partial t} + \frac{\rho_T^B}{\phi_C} \frac{\partial q_T}{\partial t} \right), \quad (20b)$$

$$\frac{\partial q_1}{\partial t} = k_1^a c_F (q_1^m - q_1) - k_1^d c_{OH} q_1, \quad (20c)$$

$$\frac{\partial q_2}{\partial t} = k_2^a c_F (q_2^m - q_2) - \kappa_2^d q_2, \quad (20d)$$

$$\frac{\partial q_T}{\partial t} = k_T^a c_F (q_T^m - q_T) - k_T^d c_{OH} q_T, \quad (20e)$$

where  $D_F$  and  $D_{OH}$  denote the effective diffusivities of  $F^-$  and  $OH^-$ , respectively, and  $\phi_C$  is the porosity of the MRC–TMRC mixture, given by  $\phi_C := (1 - f)\phi_M + f\phi_T$ , with  $f$  representing the TMRC fraction in the mixture. The effective diffusivities are not the static



Figure 7: Column lab experimental setup.

molecular diffusivity which would be  $\mathcal{O}(10^{-9})$ , rather they incorporate the effect of slow flow dispersion, hence ‘effective’. The numeric values for these are taken from Levenspiel [31], to be  $D_F = D_{OH} = 2.9 \times 10^{-7} \text{ m}^2/\text{s}$ .

The filter is assumed to be initially free of  $F^-$  ions, but not of  $OH^-$  ions. Thus, at  $t = 0$ , the initial conditions are:

$$q_1 = 0, \quad q_2 = 0, \quad q_T = 0, \quad c_F = 0, \quad \text{and} \quad c_{OH} = c_{OH}^f. \quad (20f)$$

Following the analysis in Pearson [45] and as discussed in Aguarales et al. [1], we impose Dankw-ert’s boundary condition at the inlet and a zero flux condition at the outlet:

$$vc_{\ddagger}(0, t) - D_{\ddagger} \frac{\partial c_{\ddagger}}{\partial z} \Big|_{z=0} = vc_{in}, \quad \text{and} \quad \frac{\partial c_{\ddagger}}{\partial z} \Big|_{z=L} = 0, \quad \text{for all } t, \quad (20g)$$

where  $\ddagger$  denotes either F or OH, and  $c_{in}$  represents the corresponding inlet concentration of  $F^-$ . We refer to the model for the MRC–TMRC mixture, defined by Equations (20), as the CB-MT model. All numerical solutions are obtained using MATLAB<sup>®</sup>’s built-in initial-boundary value problem solver, `pdepe`.

To assess the performance of the CB-MT model, we consider two sets of column breakthrough data: (i) three breakthrough curves with varying inlet fluoride concentrations  $c_F^f \in \{5 \pm 0.5 \text{ mg/l}, 10 \pm 0.5 \text{ mg/l}, 15 \pm 0.5 \text{ mg/l}\}$  at a fixed flow rate of 30 l/day (Figure 8, left, brown to orange), and (ii) three breakthrough curves with varying flow rates  $Q \in \{30 \text{ l/day}, 40 \text{ l/day}, 50 \text{ l/day}\}$  at a fixed fluoride concentration of  $10 \pm 0.5 \text{ mg/l}$  (Figure 8, right, blue to yellow). One experiment is repeated across both sets (highlighted in grey in Tables III and IV). In all experiments, the mass ratio of MRC to TMRC is held approximately constant at 40:1, and the filter height is around 0.1 m.

As discussed in the last paragraph of §II B 1, the model is sensitive to small variations in input parameters. To account for this, we permit slight deviations in certain experimental conditions during the fitting process. Specifically, the TMRC fraction,  $f$ , which is nominally 1/41, is allowed to vary within the range  $f \in (0.95/41, 1.05/41)$ , while the column height  $L$  such that  $L \in (0.095, 0.105)\text{m}$ . Inlet fluoride concentrations are also fitted within their experimental uncertainty of  $\pm 0.5\text{mg/l}$ . All other parameters are held fixed.

Figure 8 compares the model predictions with experimental breakthrough data; the left panel shows results for varying  $c_F^f$  and the right panel for varying flow rate  $Q$ . The CB-MT model uses

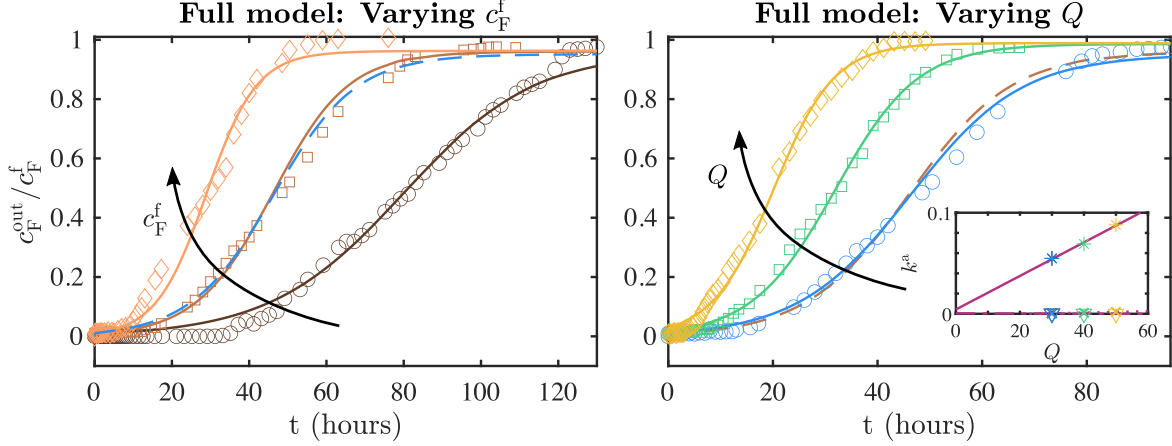


Figure 8: Breakthrough curves for a column filter composed of a mixture of MRC and TMRC in an approximate mass ratio of 40:1 (MRC:TMRC), compared to the CB-MT model predictions (*cf.* Equations 20). **Left:** Experimental data and model fits for three inlet fluoride concentrations,  $c_F^f = 5.44$  mg/l (circles), 9.5 mg/l (squares), and 14.5 mg/l (diamonds), at a fixed flow rate of 30 l/day. **Right:** Experimental and model results for three flow rates,  $Q \in \{30 \text{ l/day}, 40 \text{ l/day}, 50 \text{ l/day}\}$  (circles, squares and diamonds, respectively), with an approximate  $c_F^f = 10$  mg/l (see Table III for precise values). The inset on the right panel displays the fitted values of the forward reaction rates:  $k_T^a$  (asterisks),  $k_1^a$  (downward facing triangles), and  $k_2^a$  (crosses) and a linear best fit for each  $k^a$ . To highlight the repeated experiment, dashed lines indicate the model fit based on the other data set: the brown curve from the left panel is shown as a dashed brown line in the right panel, and the blue curve from the right is shown as dashed blue in the left.

the intrinsic parameters as determined from the isotherm fitting:  $K_1$ ,  $q_M^m$ ,  $q_2^m/q_M^m$ ,  $q_T^m$ . Their values are given in Tables I and II. The three kinetic adsorption parameters  $k_T^a$ ,  $k_1^a$ , and  $k_2^a$  are treated as fitting parameters for the column study. For each individual experiment, we also fit  $f$ ,  $L$ , and  $c_F^f$  within their respective bounds.

Fitting is performed by minimising the SSE using MATLAB<sup>®</sup>'s `lsqcurvefit` function, which employs local optimisation. Due to the high dimensionality of the parameter space, this approach is significantly more computationally efficient than global optimisation methods. To ensure convergence to physically reasonable values, parameter ranges were manually constrained before optimisation.

For the set of experiments with varying  $c_F^f$ , the forward reaction rates,  $k^a$  are fitted globally across all three breakthrough curves, due to the assumption that the  $k^a$  values are independent of inlet fluoride concentration. In contrast, for the set of experiments with varying  $Q$ , the  $k^a$  values

Optimised and goodness of fit parameters for column filter: Full model							
Param.	Feed concentration (approx)			Flow rate			Units
	5 mg/l	10 mg/l	15 mg/l	30 l/day	40 l/day	50 l/day	
$k_T^a$	0.0594			0.0548	0.0691	0.0880	l/(mol·s)
$k_1^a$	$2.19 \times 10^{-4}$			$2.73 \times 10^{-4}$	$1.01 \times 10^{-4}$	$1.11 \times 10^{-4}$	l/(mol·s)
$k_2^a$	$2.03 \times 10^{-4}$			$5.29 \times 10^{-4}$	$1.02 \times 10^{-3}$	$1.89 \times 10^{-3}$	l/(mol·s)
$c_F^f$	5.44	9.50	14.5	9.50	9.84	10.5	mg/l
	$2.86 \times 10^{-4}$	$5.00 \times 10^{-4}$	$7.63 \times 10^{-4}$	$5.00 \times 10^{-4}$	$5.18 \times 10^{-4}$	$5.53 \times 10^{-4}$	mol/l
$f$	1.05/41	1.05 /41	1.04/41	1.05/41	1.02 /41	0.950/41	–
$L$	0.105	0.105	0.101	0.105	0.104	0.0950	m
SSE	0.06316	0.03098	0.04832	0.02234	0.01490	0.02548	–
$R^2$	0.9930	0.9956	0.9916	0.9966	0.9978	0.9962	–

Table III: Fitted parameters and corresponding goodness-of-fit metrics for the chemically based combined MRC and TMRC model (CB-MT, Eqs. 20a). The fraction of TMRC is denoted  $f$  and the bed height  $L$ . Note that the SSE has been normalised using the precise inlet concentration (*i.e.*, the values of  $c_F^f$  given in this table).

are fitted individually since it is widely reported that the forward reaction rates depend on flow rate [28, 35, 40, 44, 57]; The inset on the right panel of Figure 8 shows the fitted values for the three  $k^a$  with a linear best fit.

As shown in Figure 8, the CB-MT model accurately captures the breakthrough behaviour across all six experiments. The fit is particularly notable in the varying-concentration scenario, where a single set of kinetic parameters suffices to describe all three curves. Dashed lines highlight the repeated experiment across the two data sets, underscoring the model's consistency and predictive capability.

Note that, the relative magnitudes of the forward reaction rates  $k^a$  differ between the column and batch studies, which is expected given the distinct flow regimes. In both setups,  $k_1^a, k_2^a \ll k_T^a$ ; however in the batch experiments  $k_1^a$  is an order of magnitude greater than  $k_2^a$ , while in the column experiments  $k_2^a$  ranges from the same order of magnitude as  $k_1^a$  to an order of magnitude greater than  $k_1^a$ . One possible explanation is that the ion-exchange mechanism active in TMRC may

interfere with or suppress the ion-exchange process in MRC, thereby reducing the effective rate associated with MRC and altering the apparent values of  $k_1^a$  and  $k_2^a$ .

The quality of the model fit is high across all cases, as evidenced by  $R^2$  values exceeding 0.991 for all six breakthrough curves. Additionally, the sum of squared errors (SSE) remains below 0.063 in all cases, indicating that the cumulative deviation between the experimental data and model predictions is less than 6.32% of  $c_F^f$ . For the case of varying  $c_F^f$ — where a global fit was performed across all three curves— the SSE values are slightly higher as expected, ranging from 0.0310 to 0.0632. In contrast, for the case involving varying flow rate  $Q$ , the SSE values are smaller, ranging from 0.0149 to 0.0255. Together, the consistently high  $R^2$  values and low SSE confirm the robustness and accuracy of the model fitting.

Figure 9 shows the spatial concentration profile of fluoride along the filter length over increasing times (from yellow to blue). Two distinct timescales are evident. The first, associated with TMRC and one MRC reaction ( $q_2$ ), exhibits a near-travelling wave behaviour. The second, associated with the slower MRC physisorption process ( $q_1$ ), manifests as a gradual diagonal front visible in the later-time contours (blue shades).

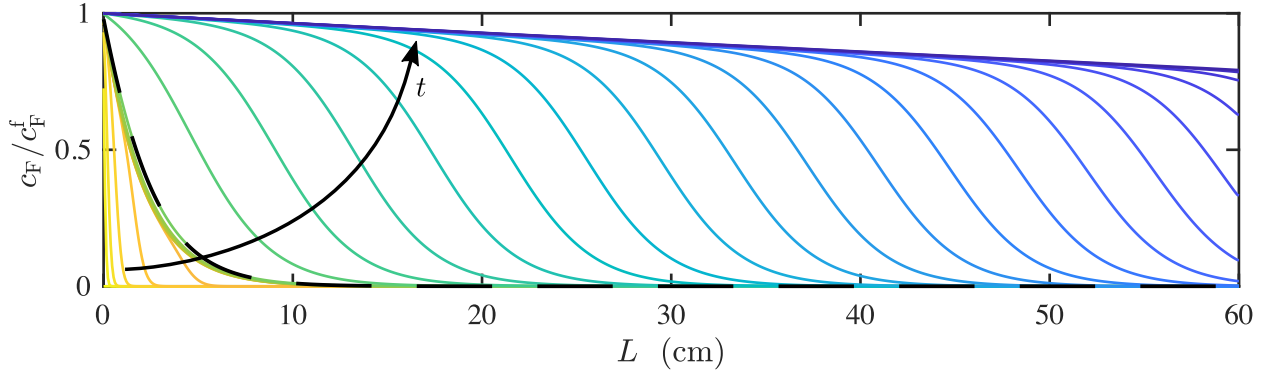


Figure 9: Normalised fluoride concentration is shown as a function of position along the filter for increasing times (yellow to blue). Here, we consider a filter of 0.6 m instead of the  $\sim 0.1$  m filter used for the experiments; a longer computational domain is considered to capture the full evolution of the concentration profile. Parameter values correspond to the case of varying feed concentration, with an inlet fluoride concentration of approximately 10 mg/l. Specifically, we use:  $k_T^a = 0.0594$ ,  $k_1^a = 2.19 \times 10^{-4}$ ,  $k_2^a = 2.03 \times 10^{-4}$ ,  $c_F^f = 9.5$  mg/l,  $f = 1.05/41$ , and  $L = 0.105$  m. The black dashed line marks the transition in time discretisation: time points before this line are spaced logarithmically, and those after are spaced linearly.

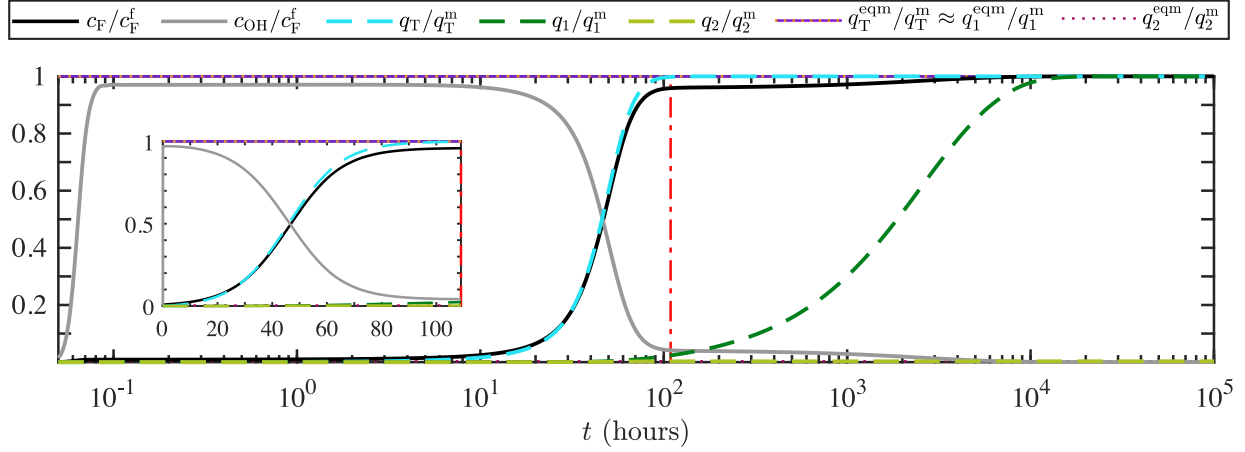


Figure 10: Outlet quantities are shown on a logarithmic time scale, using the same parameter values as in Figure 9. The equilibrium values of  $q_*$ , where  $*$  denotes either T, 1, or 2, are denoted by  $q_*^{\text{eqm}}$ . The maximum value of the ratio  $c_{\text{OH}}/c_{\text{F}}^{\text{f}} \approx 0.97$  corresponds to a peak pH of 10.7. The inset displays the same five outlet quantities plotted on a linear time scale for comparison. The vertical red dot-dash line is fixed at 109 hours, at which point  $q_2$  has reached over 95% of its equilibrium value, and  $q_{\text{T}}$  has reached approximately 99.8%.

To further understand these dynamics, Figure 10 presents the evolution of all normalised outlet quantities,  $c_{\text{F}}/c_{\text{F}}^{\text{f}}$ ,  $c_{\text{OH}}/c_{\text{F}}^{\text{f}}$ ,  $q_{\text{T}}/q_{\text{T}}^{\text{m}}$ ,  $q_1/q_1^{\text{m}}$ , and  $q_2/q_2^{\text{m}}$  versus time with the fitting parameters taken to be  $k_{\text{T}}^{\text{a}} = 0.0594$ ,  $k_1^{\text{a}} = 2.19 \times 10^{-4}$ ,  $k_2^{\text{a}} = 2.03 \times 10^{-4}$ ,  $c_{\text{F}}^{\text{f}} = 9.5 \text{ mg/l}$ ,  $f = 1.05/41$ , and  $L = 0.105 \text{ m}$ , as corresponds to the 10 mg/l experiment in the set of experiments with varying  $c_{\text{F}}^{\text{f}}$ . Initially, the outlet concentration of  $\text{OH}^-$  increases due to its production as a by-product of the chemical reactions. As  $c_{\text{OH}}$  begins to decline, a small amount of fluoride begins to appear in the outflow. Once the decline of  $c_{\text{OH}}$  accelerates,  $c_{\text{F}}^{\text{out}}$  rises more rapidly. This marks the point at which the  $q_2$  reaction becomes active; however,  $q_2$  quickly saturates to its equilibrium value, which remains far below its maximum isotherm-defined capacity, confirming that the impact of  $q_2$  on fluoride removal is minimal. Instead of  $q_2$  converging to its maximum isotherm-defined capacity,  $q_2$  converges to its equilibrium value:

$$q_2^{\text{eqm}} = \frac{q_2^{\text{m}} k_2^{\text{a}} c_{\text{F}}^{\text{f}}}{\kappa_2^{\text{d}} + k_2^{\text{a}} c_{\text{F}}^{\text{f}}}. \quad (21)$$

The minimal role played by  $q_2$  aligns with previous findings by Medellin-Castillo et al. [34] and Huyen et al. [27], who report that physisorption is strongly inhibited on negatively charged surfaces due to electrostatic repulsion.



As time progresses and the outlet concentration of  $\text{OH}^-$  vanishes, the filter nears saturation. The majority of fluoride removal is attributed to TMRC ( $q_T$ ), as evidenced by the close alignment between the cyan dashed and black solid curves in Figure 10. The contribution from  $q_1$  is marginal and becomes significant only at much later times, when it gradually saturates. At the point marked by the vertical red dot-dashed line (109 hours),  $q_2$  and  $q_T$  have reached over 95% and 99.8% of their respective equilibrium values, while only 2.3% of  $q_1$ 's maximum adsorption capacity is utilised. Full saturation of  $q_1$  (to 99%) occurs only after approximately 12,500 hours, indicating its action over a much longer timescale. This slow filling of  $q_1$  also explains the diminishing amplitude observed in the concentration profiles in Figure 9 at late times.

The maximum pH observed in the system is 10.7, occurring at  $t \approx 3.2$  hours. This pH lies just above the threshold for enhanced solubility of alumina in the presence of fluoride. According to Craig et al. [17], dissolution of aluminum hydroxide is negligible in the pH range 4–10, while Lin et al. [32] report that fluoride significantly increases alumina solubility at  $\text{pH} > 9$ . Hence, the observed maximum pH supports the assumption that dissolution in TMRC can be neglected for most of the relevant operating range, validating Equation. (13).

Analysis of all five key outlet quantities, in combination with the reaction rate parameters ( $k_1^a, k_2^a \ll k_T^a$ ; see Table III), clearly indicates that TMRC dominates fluoride removal, despite MRC being present in a much larger quantity (by mass). This is consistent with previous experimental findings by Chatterjee et al. [14], who report that TMRC exhibits more than ten times the adsorption capacity of MRC.

Given this dominance, we now consider a reduced model that includes only TMRC-based adsorption. In the following section, we fit this reduced model to experimental breakthrough curves.

#### IV. REDUCED MODEL

Motivated by the dynamics shown in Figure 10, we now consider a reduced model that neglects both components of the MRC. This simplification is justified by the minimal impact of  $q_1$  and  $q_2$  on fluoride removal, as discussed above. The resulting reduced CB-MT model comprises Equations (20a), (20b), and (20e), where we take

$$\frac{\partial q_1}{\partial t} = 0, \quad \frac{\partial q_2}{\partial t} = 0.$$

This reduction in model complexity significantly decreases the number of parameters requiring

calibration: only one fitting parameter,  $k_T^a$  is needed for the breakthrough experiments (in addition to one from the isotherm), compared to three in the full model (in addition to four from the isotherm). We assess the performance of this reduced model by fitting it to the same experimental data set, which spans a range of  $c_F^f$  and  $Q$ .

Figure 11 presents the model fits obtained using the reduced model, with the corresponding fitting parameters listed in Table IV. Visually, the fits are slightly less accurate than those obtained with the full model but still capture the dominant fluoride removal mechanisms effectively. The inset in Figure 11 again shows the fitted values of  $k_T^a$  as a function of flow rate  $Q$ , along with a linear best fit. As before, the approximately linear trend is consistent with established correlations in the literature [28, 35, 39, 40, 44, 57].

For the reduced model,  $R^2$  exceeds 0.983 for all breakthrough curves, with four of the six achieving  $R^2 > 0.991$ . The normalised SSE ranges from 0.0165 to 0.119. These consistently high  $R^2$  values and low SSE values confirm the robustness and reliability of the reduced model in describing the system's behaviour.

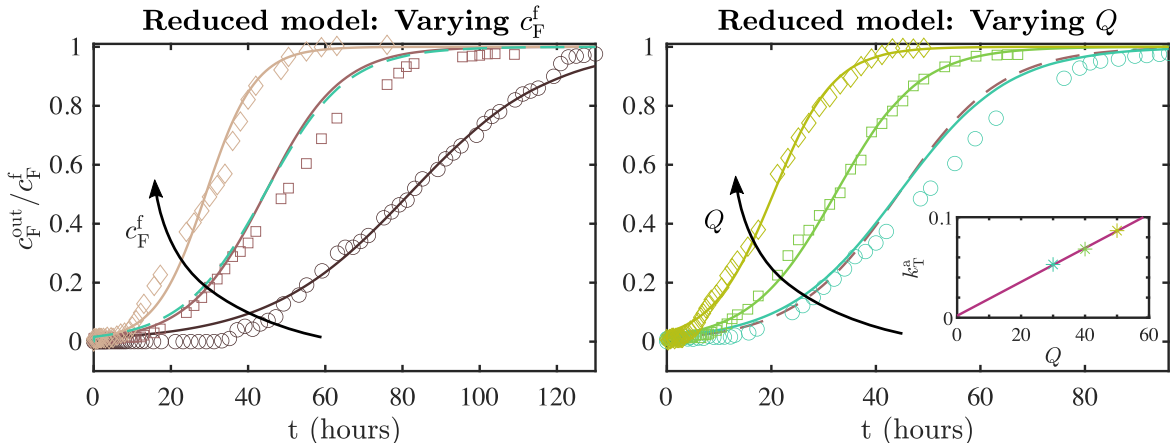


Figure 11: Breakthrough curves fitted using the reduced model (Eqs. 20a, 20b, and 20e), showing the same experimental data as in Figure 8. **Left:** Experimental data and model fits for three inlet fluoride concentrations,  $c_F^f = 5.15$  mg/l (circles), 9.5 mg/l (squares), and 14.5 mg/l (diamonds), at a fixed flow rate of 30 l/day. **Right:** Experimental and model results for three different flow rates,  $Q \in \{30, 40, 50\}$  l/day (circles, squares, and diamonds, respectively), with an inlet fluoride concentration of approximately 10 mg/l (see Table IV). The inset shows the fitted values of the forward reaction rate constant  $k_T^a$  along with a linear best-fit trend. As in Figure 8, to emphasise the repeated experiment, model fits from one panel are shown as dashed lines in the other.

Optimised and goodness of fit parameters for column filter: reduced model							
Param.	Feed concentration (approx)			Flow rate			Units
	5 mg/l	10 mg/l	15 mg/l	30 l/day	40 l/day	50 l/day	
$k_T^a$	0.0569			0.0530	0.0683	0.0866	l/(mol·s)
$c_F^f$	5.15	9.50	14.5	9.50	9.68	10.5	mg/l
	$2.71 \times 10^{-4}$	$5.00 \times 10^{-4}$	$7.63 \times 10^{-4}$	$5.00 \times 10^{-4}$	$5.09 \times 10^{-4}$	$5.50 \times 10^{-4}$	mol/l
$f$	1.05/41	1.05 /41	1.05/41	1.05/41	1.04 /41	0.950/41	–
$L$	0.105	0.105	0.105	0.105	0.104	0.0984	m
SSE	0.06301	0.1163	0.05196	0.1032	0.01648	0.02884	–
$R^2$	0.9930	0.9834	0.9910	0.9844	0.9976	0.9957	–

Table IV: Fitted parameters and corresponding goodness-of-fit metrics for the reduced model (Eqs. 20a, 20b, and 20e). As in Table III, the sum of squared errors (SSE) is normalised using the exact inlet fluoride concentration,  $c_F^f$ , as listed in this table.

Moreover, the fitted values of the operational parameters  $c_F^f$ ,  $f$ , and  $L$  are broadly consistent between the full and reduced models. This consistency further indicates that the reduced model correctly captures the key removal dynamics, and supports the notion that observed discrepancies in the input parameters reflect true deviations in the experimental setup rather than modelling artefacts.

Finally, Figure 12 shows the predicted fluoride concentration profiles within the filter over time, using the reduced model. In contrast to the full model, which exhibits two distinct timescales, the reduced model solution evolves as a near-travelling wave at large times. This behaviour is expected, as the omission of the MRC components eliminates the secondary timescale associated with slower adsorption dynamics.

## V. DISCUSSION AND CONCLUSIONS

In the present study, we carefully derived the chemically based models for fluoride adsorption using mineral-rich carbon (MRC), chemically treated mineral-rich carbon (TMRC), and their mixture. These models were validated against new experimental data, alongside experimental data

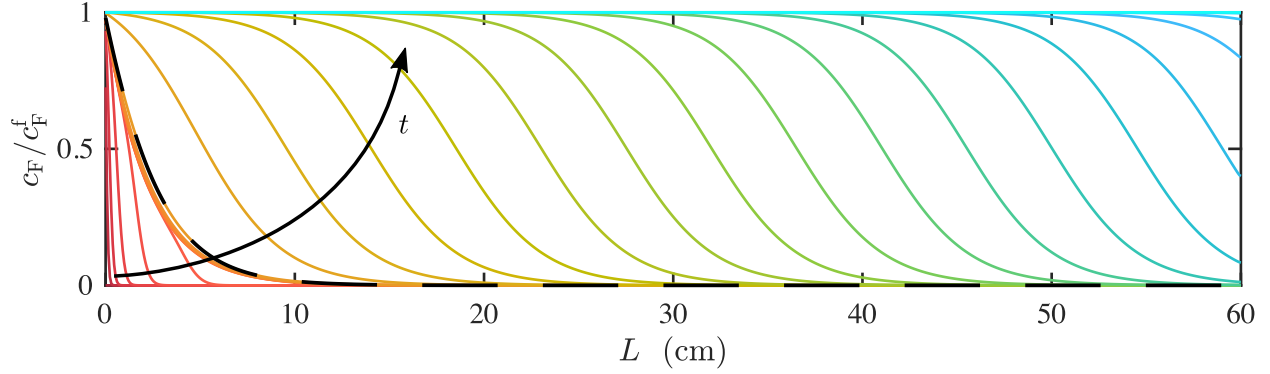


Figure 12: Normalised fluoride concentration as predicted by the reduced model as a function of position along the filter for increasing times (red to blue). We use the parameters determined for the case of varying inlet fluoride concentration around  $c_F^f \sim 10$  mg/l—that is,  $k_T^a = 0.0569$ ,  $c_F^f = 9.5$  mg/l, and  $f = 1.05/41$ . As in Figure 9, the black dashed line marks the transition in time discretisation: times before this line are spaced logarithmically, while times after are spaced linearly.

originally published in [3]. We first calibrated the individual MRC and TMRC models using batch isotherm and kinetic experiments, then extended these models to describe fixed-bed column filters. The resulting composite column model relies on four parameters that have been determined from the MRC and TMRC isotherms, leaving only three fitting parameters for the breakthrough curves.

This chemically based model showed strong predictive capabilities, particularly in reproducing breakthrough curves across varying inlet fluoride concentrations using a constant set of reaction rates, which shows that the model correctly captures the dominant chemical mechanisms occurring during the removal process. The fitting resulted in a coefficient of determination ( $R^2$ ) of over 0.991 in all cases and dimensionless sum of square errors (SSE) below 0.0632 for all curves. This shows that the model is robust and responds as expected to varying control conditions. This is indicative that the model is successfully captures the dominant removal mechanisms found in the filter.

By developing models separately for MRC and TMRC and utilising them with the individual MRC and TMRC isotherm curves, we were able to significantly reduce the parameter fitting burden for the column model. Moreover, we proposed a simplified, reduced model that considers only ion-exchange resulting from the TMRC fraction. Despite MRC outweighing the TMRC by approximately 40 times, the TMRC fraction was found to be predominately responsible for the fluoride removal. This reduced model, requiring just one fitting parameter for the breakthrough curves, still achieved excellent agreement with experimental data, with an  $R^2$  greater than 0.983

for all curves and a dimensionless SSE of less than 0.116. The simplicity of this model means that it is straightforward and inexpensive to work with numerically.

Although TMRC is a much more effective adsorbent than MRC ( $\sim 10$  times), its higher manufacturing cost and smaller grain size pose practical challenges, such as increased risk of clogging as the ratio of TMRC to MRC increases. Therefore, optimal filter design requires a careful balance between the content of MRC versus TMRC. Future work should explore the influence of varying additional operational parameters in column filters, such as filter length, cross-sectional area and ratio of MRC:TMRC, on system performance. The models presented here offer a promising foundation for future efforts aimed at predicting filter lifespan and optimising filter design. This is of particular importance for the filters currently being deployed in resource-limited settings such as rural West Bengal. Other approaches aimed at extending filter lifespan such as periodic agitation or mixing of the filter bed should also be evaluated.

Finally, further modelling and experimental studies should address the competitive adsorption between  $\text{OH}^-$  and  $\text{F}^-$ , enabling a more complete understanding of pH-dependent effects. Incorporating the influence of multiple ionic species and examining a broader pH range would help refine the mechanistic understanding of fluoride adsorption, thereby enhancing the applicability and reliability of these models in real-world settings.

## DATA

All MATLAB codes used within this manuscript can be found at:

[https://github.com/LucyAuton/Fluoride\\_removal\\_filters.git](https://github.com/LucyAuton/Fluoride_removal_filters.git)

## ACKNOWLEDGEMENTS

This publication is part of the research projects PID2023-146332OB-C21 financed by MCIN/AEI/ 10.13039/501100011033/, and by “ERDF A way of making Europe” and the CERCA Programme of the Generalitat de Catalunya. The work was also supported by the Spanish State Research Agency, through the Severo Ochoa and Maria de Maeztu Program for Centres and Units of Excellence in R&D (CEX2020-001084-M). AV is a Serra-Hunter fellow from the Serra-Hunter Programme of the Generalitat de Catalunya, and he acknowledges prior support from the Margarita Salas UPC postdoctoral grants funded by the Spanish Ministry of Universities with Euro-

pean Union funds - NextGenerationEU (UNI/551/2021 UP2021-034). Further, the authors acknowledge helpful discussions with Prof. Ian M. Griffiths of the University of Oxford, and Marc Martínez i Àvila's contributions to the initial stages of the project.

#### **AUTHOR CONTRIBUTIONS: CRediT**

**LCA:** Conceptualization; Formal analysis; Investigation; Methodology; Software; Supervision; Validation; Visualization; Writing – original draft; Writing – review and editing.

**SSR:** Data curation; Investigation; Methodology; Visualization; Writing – review and editing.

**SD:** Funding acquisition; Project administration; Resources; Supervision; Writing – review and editing.

**TGM:** Conceptualization; Funding acquisition; Investigation; Methodology; Project administration; Resources; Supervision; Writing – review and editing.

**AV:** Conceptualization; Data curation; Formal analysis; Investigation; Methodology; Software; Supervision; Validation; Writing – original draft; Writing – review and editing.

- 
- [1] M. Aguiñaga, E. Barrabés, T. G. Myers, and A. Valverde. Mathematical analysis of a Sips-based model for column adsorption. *Physica D: Nonlinear Phenomena*, 448:133690, 2023.
- [2] S. S. A Alkurdi, R. A. Al-Juboori, J. Bundschuh, and I. Hamawand. Bone char as a green sorbent for removing health threatening fluoride from drinking water. *Environment International*, 127:704–719, 2019.
- [3] L. C. Auton, M. Martínez I Àvila, S. S. Ravuru, S. De, T. G. Myers, and A. Valverde. Mathematical model for fluoride-removal filters. *Proceedings of the 22<sup>nd</sup> ECMI conference, Wroclaw*, 2023.
- [4] I. L. Balasooriya, J. Chen, S. M. Korale Gedara, Y. Han, and M. N. Wickramaratne. Applications of nano hydroxyapatite as adsorbents: a review. *Nanomaterials*, 12:2324, 2022.
- [5] M. Barathi, A. S. K. Kumar, C. U. Kumar, and N Rajesh. Graphene oxide–aluminium oxyhydroxide interaction and its application for the effective adsorption of fluoride. *RSC Advances*, 4:53711–53721, 2014.
- [6] P. Bénézeth, D. A Palmer, and D. J. Wesolowski. Dissolution/precipitation kinetics of boehmite and gibbsite: Application of a pH-relaxation technique to study near-equilibrium rates. *Geochimica et Cosmochimica Acta*, 72:2429–2453, 2008.
- [7] V. K. Bharti, A. Giri, and K. Kumar. Fluoride sources, toxicity and its amelioration: a review. *Annals of Environmental Science and Toxicology*, 2(1):021–032, 2017.
- [8] A. Bhatnagar, E. Kumar, and M. Sillanpää. Fluoride removal from water by adsorption — A review. *Chemical Engineering Journal*, 171:811–840, 2011.
- [9] K. Biswas, S. K. Saha, and U. C. Ghosh. Adsorption of fluoride from aqueous solution by a synthetic iron (III)- aluminum (III) mixed oxide. *Industrial & Engineering Chemistry Research*, 46:5346–5356, 2007.
- [10] S. Cattarin, P. Guerriero, M. Musiani, A. Tuissi, and L. Vázquez-Gómez. Electrochemical etching of NiTi alloy in a neutral fluoride solution. *Journal of The Electrochemical Society*, 156(12):C428–C434, 2009.
- [11] R. Chang. *Chemistry*. McGraw-Hill, 10 edition, Jan 2009.
- [12] S. Chatterjee. *Removal of Fluoride and Other Contaminants from Drinking Water*. PhD thesis, IIT Kharagpur, 2018.



- [13] S. Chatterjee, S. Jha, and S. De. Novel carbonized bone meal for defluoridation of groundwater: Batch and column study. *Journal of Environmental Science and Health, Part A*, 53(9):832–846, 2018.
- [14] S. Chatterjee, M. Mukherjee, and S. De. Defluoridation using novel chemically treated carbonized bone meal: batch and dynamic performance with scale-up studies. *Environmental Science and Pollution Research*, 25:18161–18178, 2018.
- [15] J. Chen, R. Yang, Z. Zhang, and D. Wu. Removal of fluoride from water using aluminum hydroxide-loaded zeolite synthesized from coal fly ash. *Journal of Hazardous Materials*, 421:126817, 2022.
- [16] K. K. Cheng, I. Chalmers, and T. A. Sheldon. Adding fluoride to water supplies. *BMJ*, 335:699–702, 2007.
- [17] L. Craig, L. L. Stillings, D. L. Decker, and J. M. Thomas. Comparing activated alumina with indigenous laterite and bauxite as potential sorbents for removing fluoride from drinking water in Ghana. *Applied Geochemistry*, 56:50–66, 2015.
- [18] L. Craig, L. L. Stillings, and D. L. Decker. Assessing changes in the physico-chemical properties and fluoride adsorption capacity of activated alumina under varied conditions. *Applied Geochemistry*, 76:112–123, 2017.
- [19] D. D. Do. *Adsorption analysis: Equilibria and kinetics*, volume 2 of *Series on Chemical Engineering*. Imperial College Press, 1998.
- [20] W.-Z. Gai, S.-H. Zhang, Y. Yang, K. Sun, H. Jia, and Z.-Y. Deng. Defluoridation performance comparison of aluminum hydroxides with different crystalline phases. *Water Supply*, 22(4):3673–3684, 2022.
- [21] S. Ghorai and K. K. Pant. Investigations on the column performance of fluoride adsorption by activated alumina in a fixed-bed. *Chemical Engineering Journal*, 98:165–173, 2004.
- [22] W.-X. Gong, J.-H. Qu, R.-P. Liu, and H.-C. Lan. Adsorption of fluoride onto different types of aluminas. *Chemical Engineering Journal*, 189–190:126–133, 2012.
- [23] W.-X. Gong, J.-H. Qu, R.-P. Liu, and H.-C. Lan. Effect of aluminum fluoride complexation on fluoride removal by coagulation. *Colloids and Surfaces A: Physicochemical and Engineering Aspects*, 395:88–93, 2012.
- [24] O. J. Hao and C. P. Huang. Adsorption characteristics of fluoride onto hydrous alumina. *Journal of Environmental Engineering*, 112:1054–1069, 1986.
- [25] J. D. Hem and C. E. Roberson. *Form and stability of aluminum hydroxide complexes in dilute solution*. Chemistry of aluminium in natural water. US Government Printing Office, 1967.

- [26] S. Huang, X. Zhang, L. Wang, D. Li, C. Zhang, L. Yang, Q. He, and B. Gao. Enhanced water defluoridation using ion channel modified hydroxyapatite: Experimental, mechanisms and DFT calculation. *Applied Surface Science*, 615:156351, 2023.
- [27] D. T. Huyen, L. N. Phat, D. X. Tien, D. P. G. Thu, and D. Q. Thoai. Bone-char from various food-waste: Synthesis, characterization, and removal of fluoride in groundwater. *Environmental Technology & Innovation*, 32:103342, 2023.
- [28] V. J. Inglezakis, M. Balsamo, and F. Montagnaro. Liquid–solid mass transfer in adsorption systems—an overlooked resistance? *Industrial & Engineering Chemistry Research*, 59:22007–22016, 2020.
- [29] Y. Jia, Z. Zhu, B.-S. and Jin, B. Sun, T. Luo, X.-Y. Yu, L.-T. Kong, and J.-H. Liu. Fluoride removal mechanism of bayerite/boehmite nanocomposites: roles of the surface hydroxyl groups and the nitrate anions. *Journal of Colloid and Interface Science*, 440:60–67, 2015.
- [30] L. S. Kaminsky, M. C. Mahoney, J. Leach, J. Melius, and M. Jo Miller. Fluoride: benefits and risks of exposure. *Critical Reviews in Oral Biology & Medicine*, 1(4):261–281, 1990.
- [31] O. Levenspiel. *Chemical Reaction Engineering*. John Wiley & Sons, third edition, 1999.
- [32] J.-Y. Lin, Y.-L. Chen, X.-Y. Hong, C. Huang, and C. P. Huang. The role of fluoroaluminate complexes on the adsorption of fluoride onto hydrous alumina in aqueous solutions. *Journal of Colloid and Interface Science*, 561:275–286, 2020.
- [33] M. Locatelli and F. Schoen. Random linkage: a family of acceptance/rejection algorithms for global optimisation. *Mathematical Programming*, 85:379–396, 1999.
- [34] N. A. Medellin-Castillo, E. Leyva-Ramos, R. and Padilla-Ortega, R. Ocampo Perez, J. V. Flores-Cano, and M. S. Berber-Mendoza. Adsorption capacity of bone char for removing fluoride from water solution. Role of hydroxyapatite content, adsorption mechanism and competing anions. *Journal of Industrial and Engineering Chemistry*, 20(6):4014–4021, 2014.
- [35] D. M. Misic, Y. Sudo, Suzuki M., and K. Kawazoe. Liquid-to-particle mass transfer in a stirred batch adsorption tank with non-linear isotherm. *Journal of Chemical Engineering of Japan*, 15(1):67–70, 1982.
- [36] D. S. Mosiman. *Probing structure-property relationships of calcium hydroxyapatite defluoridation to enhance performance*. PhD thesis, University of Illinois at Urbana-Champaign, 2021.
- [37] D. S. Mosiman, A. Sutrisno, R. Fu, and B. J. Mariñas. Internalization of fluoride in hydroxyapatite nanoparticles. *Environmental Science & Technology*, 55:2639–2651, 2021.

- [38] T. G. Myers. Is it time to move on from the Bohart-Adams model for column adsorption? *International Communications in Heat and Mass Transfer*, 159:108062, 2024.
- [39] T. G. Myers, F. Font, and M. G. Hennessy. Mathematical modelling of carbon capture in a packed column by adsorption. *Applied Energy*, 278:115565, 2020. doi:10.1016/j.apenergy.2020.115565.
- [40] T. G. Myers, A. Cabrera-Codony, and A. Valverde. On the development of a consistent mathematical model for adsorption in a packed column (and why standard models fail). *International Journal of Heat and Mass Transfer*, 202:123660, 2023.
- [41] Y. Nie, C. Hu, and C. Kong. Enhanced fluoride adsorption using Al (III) modified calcium hydroxyapatite. *Journal of Hazardous Materials*, 233–234:194–199, 2012.
- [42] J. P. Nordin, D. J. Sullivan, B. L. Phillips, and W. H. Casey. Mechanisms for fluoride-promoted dissolution of bayerite [ $\beta$ -Al(OH)<sub>3</sub>(s)] and boehmite [ $\gamma$ -AlOOH]: <sup>19</sup>F-NMR spectroscopy and aqueous surface chemistry. *Geochimica et Cosmochimica Acta*, 63(21):3513–3524, 1999.
- [43] D. L. Ozsvath. Fluoride and environmental health: A review. *Reviews in Environmental Science and Biotechnology*, 8:59–79, 2009.
- [44] A. Patmonoaji, M. A. Tahta, J. A. Tuasikal, Y. She, Y. Hu, and T. Suekane. Dissolution mass transfer of trapped gases in porous media: A correlation of Sherwood, Reynolds, and Schmidt numbers. *International Journal of Heat and Mass Transfer*, 205:123860, 2023.
- [45] J. R. A. Pearson. A note on the “Danckwerts” boundary conditions for continuous flow reactors. *Chemical Engineering Science*, 10:281–284, 1959.
- [46] C. Ren, Z. Yu, B. L. Phillips, H. Wang, J. Ji, B. Pan, and W. Li. Molecular-scale investigation of fluoride sorption mechanism by nanosized hydroxyapatite using <sup>19</sup>F solid-state NMR spectroscopy. *Journal of Colloid and Interface Science*, 557:357–366, 2019.
- [47] V. Russo, R. Tesser, M. Trifuoggi, M. Giugni, and M. Di Serio. A dynamic intraparticle model for fluid–solid adsorption kinetics. *Computers and Chemical Engineering*, 74:66–74, 2015.
- [48] V. Russo, A. D’Angelo, C. Salvi, R. Paparo, M. E. Fortunato, E. M. Cepollaro, O. Tarallo, M. Trifuoggi, M. Di Serio, and R. Tesser. Fluoride adsorption on hydroxyapatite: From batch to continuous operation. *Journal of Environmental Chemical Engineering*, 12:111973, 2024.
- [49] M. Sarkar, A. Banerjee, P. P. Pramanick, and A. R. Sarkar. Use of laterite for the removal of fluoride from contaminated drinking water. *Journal of Colloid and Interface Science*, 302:432–441, 2006.
- [50] V. Sternitzke, R. Kaegi, J.-N. Audinot, E. Lewin, J. G. Hering, and C. A. Johnson. Uptake of fluoride from aqueous solution on nano-sized hydroxyapatite: examination of a fluoridated surface layer.

- Environmental Science & Technology*, 46:802–809, 2012.
- [51] C. S. Sundaram, N. Viswanathan, and S. Meenakshi. Defluoridation chemistry of synthetic hydroxyapatite at nano scale: Equilibrium and kinetic studies. *Journal of Hazardous Materials*, 155:206–215, 2008.
  - [52] G Tomar, A Thareja, and S. Sarkar. Enhanced fluoride removal by hydroxyapatite-modified activated alumina. *International Journal of Environmental Science and Technology*, 12:2809–2818, 2015.
  - [53] S. S. Tripathy, J.-L. Bersillon, and K. Gopal. Removal of fluoride from drinking water by adsorption onto alum-impregnated activated alumina. *Separation and Purification Technology*, 50:310–317, 2006.
  - [54] M. S Tung and D. Skrtic. Interfacial properties of hydroxyapatite, fluoroapatite and octacalcium phosphate. *Monographs in Oral Science*, 18 (Octacalcium Phosphate):112–129, 2001.
  - [55] Z. Ugray, L. Lasdon, J. Plummer, F. Glover, J. Kelly, and R. Martí. Scatter search and local NLP solvers: A multistart framework for global optimization. *INFORMS Journal on Computing*, 19(3): 328–340, 2007.
  - [56] M. Vithanage, L. Jayarathna, A. U. Rajapaksha, C. B. Dissanayake, M. S. Bootharaju, and T. Pradeep. Modeling sorption of fluoride on to iron rich laterite. *Colloids and Surfaces A: Physicochemical and Engineering Aspects*, 398:69–75, 2012.
  - [57] N. Wakao and T. Funazkri. Effect of fluid dispersion coefficients on particle-to-fluid mass transfer coefficients in packed beds: Correlation of Sherwood numbers. *Chemical Engineering Science*, 33: 1375–1384, 1978.
  - [58] G. Wendimu, F. Zewge, and E. Mulugeta. Aluminium-iron-amended activated bamboo charcoal (AIAABC) for fluoride removal from aqueous solutions. *Journal of Water Process Engineering*, 16: 123–131, 2017.
  - [59] World Health Organisation (WHO). Preventing disease through healthy environments. Inadequate or excess fluoride: a major public health concern. WHO publication: Chemical Safety and Health Unit, WHO/CED/PHE/EPE/19.4.5, 2019.
  - [60] X. Yang, Z. Sun, D. Wang, and W. Forsling. Surface acid–base properties and hydration/dehydration mechanisms of aluminum (hydr)oxides. *Journal of Colloid and Interface Science*, 308:395–404, 2007.